



**CHALMERS**  
UNIVERSITY OF TECHNOLOGY

## **Facile Epitaxial Growth of Novel Nanoscale Ag-MAFs on Reverse Osmosis Membranes: Enhancing Performance, Antibacterial Activity, and**

Downloaded from: <https://research.chalmers.se>, 2026-05-16 04:35 UTC

Citation for the original published paper (version of record):

Seyedpour, S., Karami, P., Khoshhal Salestan, S. et al (2025). Facile Epitaxial Growth of Novel Nanoscale Ag-MAFs on Reverse Osmosis Membranes: Enhancing Performance, Antibacterial Activity, and (Bio)fouling Resistance. *ACS Omega*, 10(26): 28191-28209. <http://dx.doi.org/10.1021/acsomega.5c02816>

N.B. When citing this work, cite the original published paper.

# Facile Epitaxial Growth of Novel Nanoscale Ag-MAFs on Reverse Osmosis Membranes: Enhancing Performance, Antibacterial Activity, and (Bio)fouling Resistance

Seyedeh Fatemeh Seyedpour, Pooria Karami,\* Saeed Khoshhal Salestan, Sadegh Aghapour Aktij, Upasana Singh, Suyenna Huang, Jia Wei Chew, Ahmad Rahimpour, David Wishart,\* and Mohtada Sadrzadeh\*

Cite This: <https://doi.org/10.1021/acsomega.5c02816>

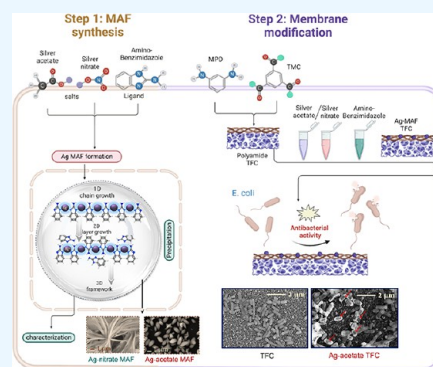
Read Online

ACCESS |

Metrics & More

Article Recommendations

**ABSTRACT:** The increasing demand for advanced thin-film composite (TFC) membranes stems from the limitations of current commercial membranes, particularly their vulnerability to biofouling. In this study, novel silver-based metal-azolate frameworks (Ag-MAFs) were grown insitu on the surface of TFC reverse osmosis (RO) membranes. This functionalization resulted in a 45% increase in permeate flux without compromising salt rejection (97.6%) compared to pristine TFC membranes. The surface functionalization process is rapid, non-destructive, and employs eco-friendly solvents, silver salts, and amino-benzimidazole ligands, enabling repeatable modifications without affecting separation efficiency. The successful integration of Ag-MAFs onto the membrane surface was confirmed through comprehensive chemical characterization, including Fourier transform infrared (FTIR) spectroscopy, X-ray photoelectron spectroscopy (XPS), and energy dispersive X-ray (EDX) analysis. Notably, Ag-MAFs demonstrated strong stability, with no detectable leaching or detachment after 20 days of continuous water immersion. Morphological analysis using scanning electron microscopy (SEM) and confocal microscopy revealed that Ag-MAFs nanoparticles imparted robust antibacterial activity, reducing live bacterial populations by nearly 99%. Filtration tests showed that Ag-MAFs functionalized membranes exhibited superior fouling resistance and higher water recovery ratios than pristine membranes during a 10 h filtration cycle. This study presents a scalable and reproducible approach for developing advanced antibiofouling TFC membranes capable of long-term operation, eliminating the need for module disassembly and enhancing membrane longevity in practical applications.



## 1. INTRODUCTION

The reverse osmosis (RO) process is widely utilized for desalination and industrial wastewater treatment due to its high separation efficiency.<sup>1</sup> Polyamide thin-film composite (PA-TFC) membranes are the predominant choice for RO applications owing to their excellent water permeability and salt rejection properties.<sup>2</sup> However, biofouling remains a major challenge, leading to increased energy consumption, reduced membrane lifespan, and higher operational costs.<sup>3,4</sup> Biofouling occurs due to the adhesion of microorganisms and the secretion of extracellular polymeric substances (EPS), which facilitate biofilm formation on the membrane surface.<sup>5</sup> Even with rigorous pretreatment measures achieving a 99.9% bacterial reduction, residual bacteria can still proliferate and form biofilms.<sup>6</sup> Moreover, conventional pretreatment agents such as active chlorine compounds, while effective in mitigating biofouling, pose a risk of degrading the polyamide layer due to their strong oxidizing nature.<sup>3</sup> Thus, developing RO membranes with

enhanced biofouling resistance is crucial for improving process sustainability and cost efficiency.

Biofouling resistance is closely linked to membrane surface properties, influencing interactions between foulants and the membrane. Surface modifications can impart antibacterial properties through contact-killing and release-killing mechanisms, thereby preventing bacterial attachment and proliferation.<sup>7</sup> Various approaches have been explored to enhance the antibacterial properties of RO membranes, including the incorporation of antimicrobial agents within the membrane matrix,<sup>8</sup> surface coatings,<sup>9</sup> and chemical grafting.<sup>10</sup> Among these, insitu surface modification via covalent bonding has

Received: March 27, 2025

Revised: June 6, 2025

Accepted: June 11, 2025

emerged as a promising and scalable strategy due to its long-term stability under operational conditions. Antibacterial materials such as silver nanoparticles (Ag NPs), graphene oxide, carbon nanotubes, and metal–organic frameworks (MOFs) have been extensively studied to mitigate biofouling.<sup>11</sup> Ag NPs, in particular, are widely recognized for their strong and broad-spectrum antibacterial properties.<sup>12</sup> However, challenges such as nanoparticle aggregation and excessive Ag loading can negatively impact membrane performance, highlighting the need for precise functionalization strategies.<sup>13,14</sup> Moreover, there are still technical drawbacks associated with the inevitable release of residual solvents and chemicals, which pose environmental and health risks. The modification process often requires multiple sequential reaction steps, increasing both time and cost.<sup>15</sup> Excessive use of Ag NPs can also lead to particle aggregation, reducing their antibacterial effectiveness.<sup>16</sup> While capping agents are commonly employed to improve NPs dispersion, they may inadvertently hinder antibacterial activity and immobilization efficiency due to interference from organic materials on the NP surface.<sup>17</sup> Furthermore, Ag NPs modification can degrade membrane performance, negatively impacting solute rejection and water flux.<sup>18</sup>

Nanostructured Ag-based metal-azolate frameworks (MAFs) have garnered attention for their tunable antibacterial properties, leveraging the biocidal activity of both silver ions and azolate ligands.<sup>19</sup> MAFs are a subclass of metal coordination polymers composed of a metal core and a five-membered heterocyclic azolate ligand.<sup>20</sup> Nitrogen-containing heterocyclic structures (NHS's) coordinate with metals via strong  $\sigma$ -donation and weak  $\pi$ -acceptor interactions. Primary bonding involves  $\sigma$ -donation to the metal's d orbitals,<sup>21</sup> thereby forming stable adducts with metal centers.<sup>22</sup> Moreover, NHS's exhibit a degree of  $\pi$ -acceptor behavior and stabilize electron-deficient metals through  $\pi \rightarrow d$  donation and electron-rich metals via  $d \rightarrow \pi^*$  backbonding.<sup>23</sup> Among various NHS ligands used in coordination structures containing Ag ions, multidentate nitrogen donors, such as benzimidazole, can form promising architectures. The Ag<sup>+</sup> ion has a strong affinity for N-donor ligands, reacting with them through coordination bonds. A study on Ag–NHS complexes revealed that NHS's are strong electron donors but are relatively weak  $\pi$ -acceptors.<sup>24</sup> When Ag is incorporated as the metal center, these frameworks exhibit potent antibacterial activity through controlled Ag<sup>+</sup> ion release and the biocidal effects of imidazole-based ligands.<sup>20,25</sup> The coordination chemistry of nitrogen-containing heterocyclic structures (NHSs) plays a crucial role in the stability and antibacterial efficacy of Ag-based complexes.<sup>21–23</sup> Benzimidazole, a nitrogen-containing heterocyclic compound, has been widely studied for its antibacterial, antifungal, and antiviral properties.<sup>26</sup> It functions by binding to bacterial transpeptidase enzymes, thereby disrupting cell wall biosynthesis and leading to bacterial cell death.<sup>27</sup> Additionally, benzimidazole-based derivatives have demonstrated potent antibacterial effects against a broad range of pathogens.<sup>28</sup>

This study aims to develop novel biofouling-resistant RO membranes by incorporating Ag-amino-benzimidazole MAFs onto the membrane surface. A green surface modification approach was employed by carefully selecting metal salts, organic linkers, and solvents to ensure an eco-friendly process. The deposition of Ag-MAFs on the membrane imparts antibacterial properties, while the hydrophilic amine functional groups enhance water flux and minimize fouling tendencies. The impact of this *in situ* surface modification was assessed by

characterizing the membranes' surface morphology, physico-chemical properties, and transport performance. Furthermore, the antibacterial efficacy of the Ag-MAFs-modified membranes was examined through confocal and SEM imaging, providing insights into bacterial adhesion and viability. This modification strategy is compatible with high-throughput manufacturing processes used in commercial RO membrane production, ensuring enhanced antibiofouling properties without compromising membrane permeability.

## 2. MATERIALS AND METHODS

**2.1. Materials.** Silver acetate (99.0%), silver nitrate (99.0%), amino-benzimidazole ( $\geq 95.0\%$ ), and ethanol ( $>99\%$ ) were purchased from Sigma-Aldrich and used for surface modification. TFC RO membranes were supplied by GreEnvi Corp. (Canada). Sodium chloride (NaCl, 99.5%, Sigma-Aldrich) was utilized to prepare the feed solution. Bovine serum albumin (BSA), from Sigma-Aldrich, served as a model organic foulant. Luria–Bertani (LB) broth (Sigma-Aldrich) was used for the bacterial cell culture. *Escherichia coli* (BL21(DE3)) was used as a Gram-negative bacterium. Propidium iodide (PI) and SYTO9 (Molecular Probes) were purchased from Thermo Fisher Scientific. All chemicals were of analytical grade and used without further purification.

**2.2. Synthesis of Ag-MAFs.** Two types of Ag-MAFs were synthesized for this study: one derived from the nitrate salt and the other from the acetate salt. An identical procedure was employed for both cases. For nitrate-based MAFs, 0.15 g of silver nitrate (AgNO<sub>3</sub>) was dissolved in 30 mL of deionized water. Then, 0.1 g of amino-benzimidazole was dissolved in 25 mL of ethanol. Before synthesis, both solutions were thoroughly stirred and sonicated to achieve a homogeneous solution without agglomeration. The organic solution was added to the silver salt solution while stirring to induce precipitation. The mixture was stirred for 20 min to complete the reaction. Then, the precipitate was filtered and washed twice with 50 mL of fresh ethanol to remove any unreacted reagents. The same procedure was followed for synthesizing the acetate-based MAFs with different quantities of silver salt (0.12 g).

**2.3. Surface Modification of TFC Membrane.** The polyamide TFC RO membranes were prepared via an interfacial polymerization (IP) process between MPD and TMC on the surface of the poly(ether sulfone) (PES) substrate. The polyamide TFC membrane was fabricated by soaking the PES substrate in an aqueous solution containing 2 wt % MPD, 2 wt % CSA, 1 wt % TEA, and some additives for 2 min. The excess MPD solution was then carefully discarded from the membrane surface with a roller. The MPD-saturated membrane was immersed in a 0.1 wt/v % TMC solution containing *n*-hexane and an additive for 30 s to allow polyamide layer formation. Subsequently, the membrane was subjected to an oven at 80 °C for 5 min for post-thermal treatment. The IP reaction, based on the Schotten–Baumann mechanism, tends to be rapid and unregulated, leading to a nonuniform cross-linked polyamide active layer.<sup>29</sup> The thermal treatment applied post-IP primarily serves to enhance polymer chain cross-linking, remove residual solvents, and improve membrane structural integrity, rather than driving the initial polymerization itself. Ag-MAFs were *in situ* deposited on the TFC membrane surface through a rapid and environmentally friendly procedure at room temperature. The residual acyl chloride functional groups present on the surface of the fresh TFC membrane undergo hydrolysis, transforming into carboxyl groups.<sup>30,31</sup> The RO membranes have many carboxylic

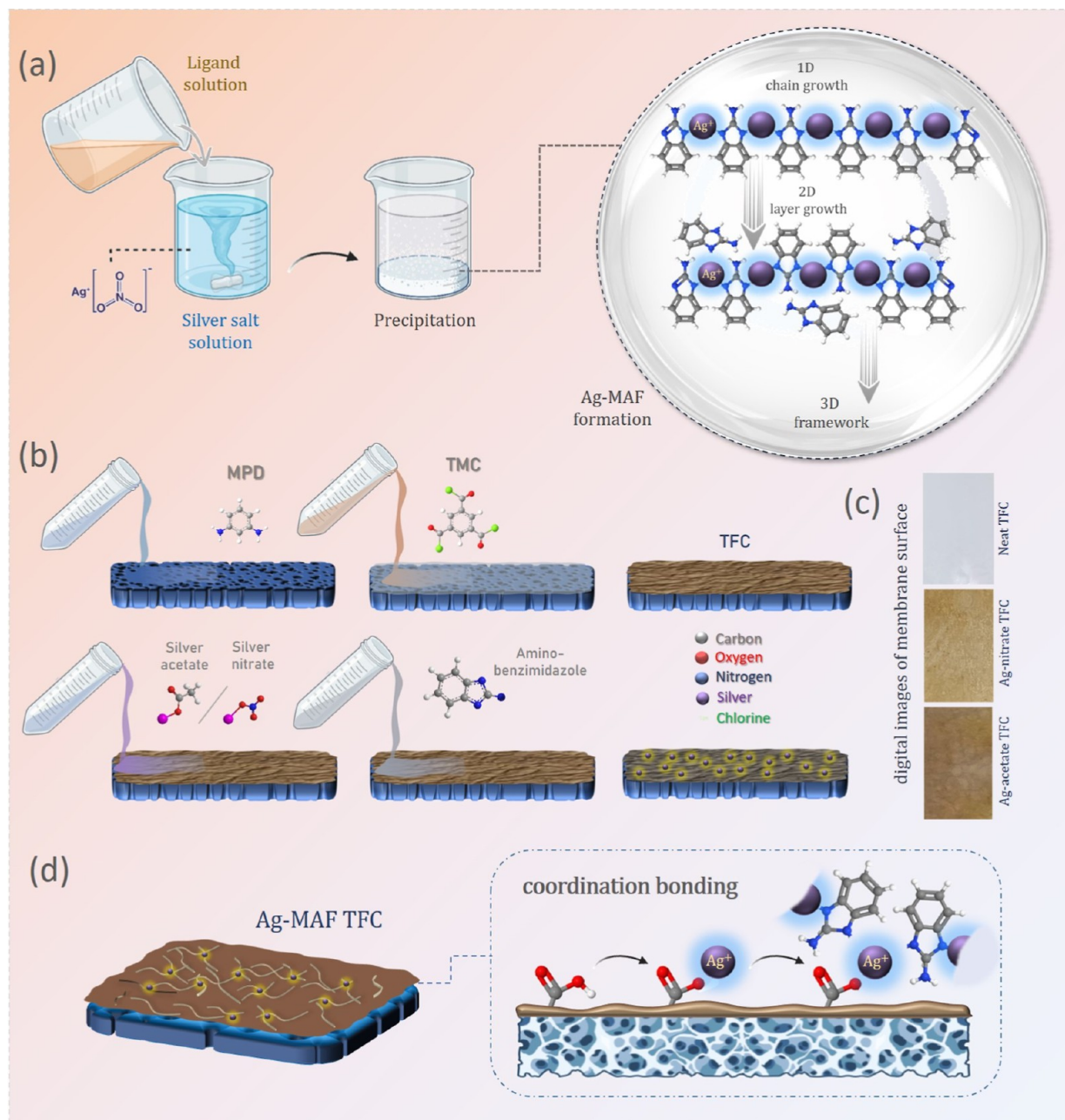


**Figure 1.** (a) The schematic illustration of Ag-MAFs synthesis. Ag-MAFs were synthesized separately for chemical and morphological characterizations, (b) IP reaction between MPD (*m*-phenylenediamine) and TMC (trimesoyl chloride) to fabricate TFC membranes and in-situ surface functionalization of TFC membranes with Ag-MAFs, (c) digital images of the synthesized membranes, and (d) the chemical interactions of carboxylic groups and Ag-MAFs on the polyamide surface.

groups spread over the polyamide surface. These carboxyl groups, carrying a negative charge, serve as active deposition sites for further modification. The strong interaction between the negatively charged moieties of the polyamide surface and the positively charged Ag ions leads to the adhesion of Ag particles to the membrane surface.<sup>32</sup> Once the Ag ions are anchored to these sites, the amino-benzimidazole linker coordinates with the Ag atoms through a robust chemical interaction between the Ag ions and the amino-benzimidazole ligand.<sup>20</sup> This interaction facilitates the formation of Ag-MAFs on the Ag-anchored sites, creating a functionalized membrane surface.

The membrane surface was treated with silver salt, followed by ligand solutions to attach Ag-MAFs covalently. First, the membrane was contacted with 100 mL of aqueous solution

containing 0.48 g silver nitrate (or 0.38 g silver acetate) for 30 min to allow the attachment of silver ions. Afterward, the silver-treated surface was exposed to 100 mL ethanol solution containing 0.33 g of amino-benzimidazole for 30 min to form Ag-MAFs. The whole surface modification process was conducted at ambient temperature. The surface of modified membranes featured a brownish color. The membranes were washed with water to remove unattached Ag-MAFs and stored in deionized water before characterizations.

Figure 1- illustrates the schematic representation of (a) the synthesis of Ag-MAFs, (b) the surface functionalization of TFC membranes by in-situ deposition of Ag-MAFs, (c) the color changes seen on the membrane surface, and (d) the interaction of carboxylic groups and Ag-MAFs over the membrane surface.

In Figure 1c, the TFC membrane undergoes a color change from white to brown, observed in both Ag-nitrate MAFs and Ag-acetate MAFs membranes. This color change signifies the successful deposition of Ag-MAFs on the TFC surface.

### 3. CHARACTERIZATION

**3.1. Evaluation of the Membrane Transportation Properties.** The transport properties of the pristine and surface-modified RO membranes were evaluated using a lab-scale cross-flow filtration setup (Sterlitech Corp., USA) to measure water flux and salt rejection. The system has a flow cell with an effective surface area of 20.6 cm<sup>2</sup>. The feed solution is a 2000 ppm NaCl solution with a flow rate of 4.5 L·min<sup>-1</sup>. The filtration setup was equipped with a circulating water bath (Isotemp3013, Fisher Scientific) to monitor the feed temperature. The water flux was measured by an electronic balance connected to a computer. An online lab-scale conductivity meter was used to record the conductivity of the feed and permeate solutions. Each experiment was conducted for 8 h at room temperature. A transmembrane pressure of 220 psi was applied in all experiments. The filtration tests were repeated three times to ensure accuracy and to record the average results. The water flux ( $J_w$ ) was determined by the following equation

$$J_w = \frac{\Delta m}{A \cdot \Delta t \cdot \rho} \quad (1)$$

where  $\Delta m$  is the mass difference of permeate solution,  $\rho$  is the permeate density,  $A$  is the effective membrane surface area, and  $\Delta t$  is the time interval. The salt rejection was calculated by measuring the conductivity of the feed and permeate solutions by the following equation

$$J_s = \left( 1 - \frac{C_p}{C_f} \right) \times 100 \quad (2)$$

where  $J_s$  represents membrane water flux.  $C_p$  and  $C_f$  represent the permeate and feed conductivity, respectively.

**3.2. Chemical and Morphological Characterizations of Synthesized Ag-MAFs and TFC Membranes.** The Ag-MAFs synthesized in this study represent a novel subclass, with bulk synthesis enabling structural confirmation via XRD, which is unsuitable for thin-film membranes due to substrate interference. In situ growth on TFC membranes was verified through XPS, FTIR, SEM, and TEM imaging. Although both synthesis routes follow the same chemistry, differences in nucleation environments result in distinct morphologies, in which bulk synthesis yields well-defined crystals, while in situ growth produces surface-confined structures due to substrate interactions. The functional groups of Ag-MAFs, pristine, and surface-modified membranes were identified by attenuated total reflectance–Fourier transform infrared (ATR–FTIR, using Agilent Technologies, Cary 600 series FTIR spectrometer) spectra. Ag-MAFs were further analyzed using powder X-ray diffraction (PXRD, Bruker D8 XRD) at ambient temperature. A copper-based anode ( $\lambda = 1.5406 \text{ \AA}$ ) was used to record the diffraction pattern of the samples in the range of 4° to 70° with a step size of 0.05°. The PXRD data were first interpolated using a sixth-order polynomial to enhance resolution, followed by baseline adjustment to the interpolated graph to identify the crystalline structure of the synthesized Ag-MAFs and index the peaks. The background signal was then removed to yield a clearer diffraction pattern. Subsequently, the TREOR90 algorithm,<sup>33</sup> integrated within the Materials Studio software

(MS 2020), was utilized to identify characteristic peaks and approximate the crystalline structure of the samples. The elemental composition (C, O, N, and Ag) and chemical bonds of synthesized membranes were analyzed by X-ray photoelectron spectroscopy (XPS, Kratos AXIS ULTRA XPS equipped with a monochromatic aluminum  $K\alpha$  X-ray source, energy of 1486.71 eV), providing information from 1–10 nm of the membrane surface in the range of 0–1100 eV with high-resolution scans of 0.1 eV.

Field-emission scanning electron microscopy (FE-SEM, Zeiss Sigma 300 VP) equipped with an energy-dispersive X-ray spectrometer (EDX) was used to image the Ag-MAFs and the morphologies of the synthesized membranes. For FE-SEM imaging, all samples were first coated with carbon, and the top surface was imaged at a magnification of 5000–30,000 $\times$ . Transmission electron microscopy (TEM, Philips/FEI Morgagni 268, The Netherlands) was used to image the cross-section structure of the membranes. Atomic force microscopy (AFM, Bruker Dimension Icon, USA) was used to determine the surface roughness using tapping mode at room temperature. The roughness of the membrane surfaces was measured by ICSPI nGauge software and reported as average roughness ( $R_a$ ) and root-mean-square roughness ( $R_q$ ).

The membrane surface hydrophilicity was evaluated by contact angle measurements (Kruss Model DSA 100E, Hamburg, Germany) using the sessile drop method. The release of silver ions from the Ag-modified membranes was evaluated by inductively coupled plasma optical emission spectrometry (ICP–OES, Thermo iCAP6300). The experiment details are reported in our previous studies.<sup>34,35</sup>

**3.3. Harsh Condition Experiment and pH Stability.** In industrial applications, fouled RO membranes are typically cleaned using acidic or alkaline solutions to restore their separation performance.<sup>36</sup> However, the cleaning process may compromise the TFC layer integrity, especially when the surface is further modified. To evaluate the stability of Ag-MAFs-modified TFC membranes, two types of experiments were conducted: pH stability testing and high-temperature performance assessment. The acid/alkaline resistance of the Ag-MAFs-modified TFC membranes was evaluated by a long-term immersion test. The membrane samples were immersed in HCl (pH = 3) or NaOH (pH = 12) solutions for 7 days at room temperature, exposing the active layer to the aqueous solutions.<sup>37</sup> The pH was adjusted using 1 M HCl and 5 M NaOH.<sup>38</sup> After exposure, the membranes were rinsed with DI water to remove the excess NaOH or HCl remaining on the surface and neutralize the pH. Immediately afterward, the membrane samples were subjected to SEM imaging and EDX mapping to examine potential structural, compositional, or morphological changes. For high-temperature stability, the membranes were tested at 75 °C under a transmembrane pressure of 220 psi for 6 h. The salt rejection was recorded at the end of the experiment.

**3.4. Antibacterial Activity Assessment of the Membranes.**  
**3.4.1. Bacteria Strains and Suspension Preparation.** The antibacterial properties of the pristine and Ag-MAFs functionalized membranes were assessed using the Gram-negative *E. coli* BL21 (D3) strain. The cells were cryopreserved (via liquid nitrogen flash freezing) using a 70% glycerol solution and stored in a freezer maintained at –80 °C until needed. Upon thawing and revival, the optical density of the cryopreserved cells was between 0.8 and 1.0 at 600 nm, indicating a healthy population of viable cells. To prepare enough cells to conduct

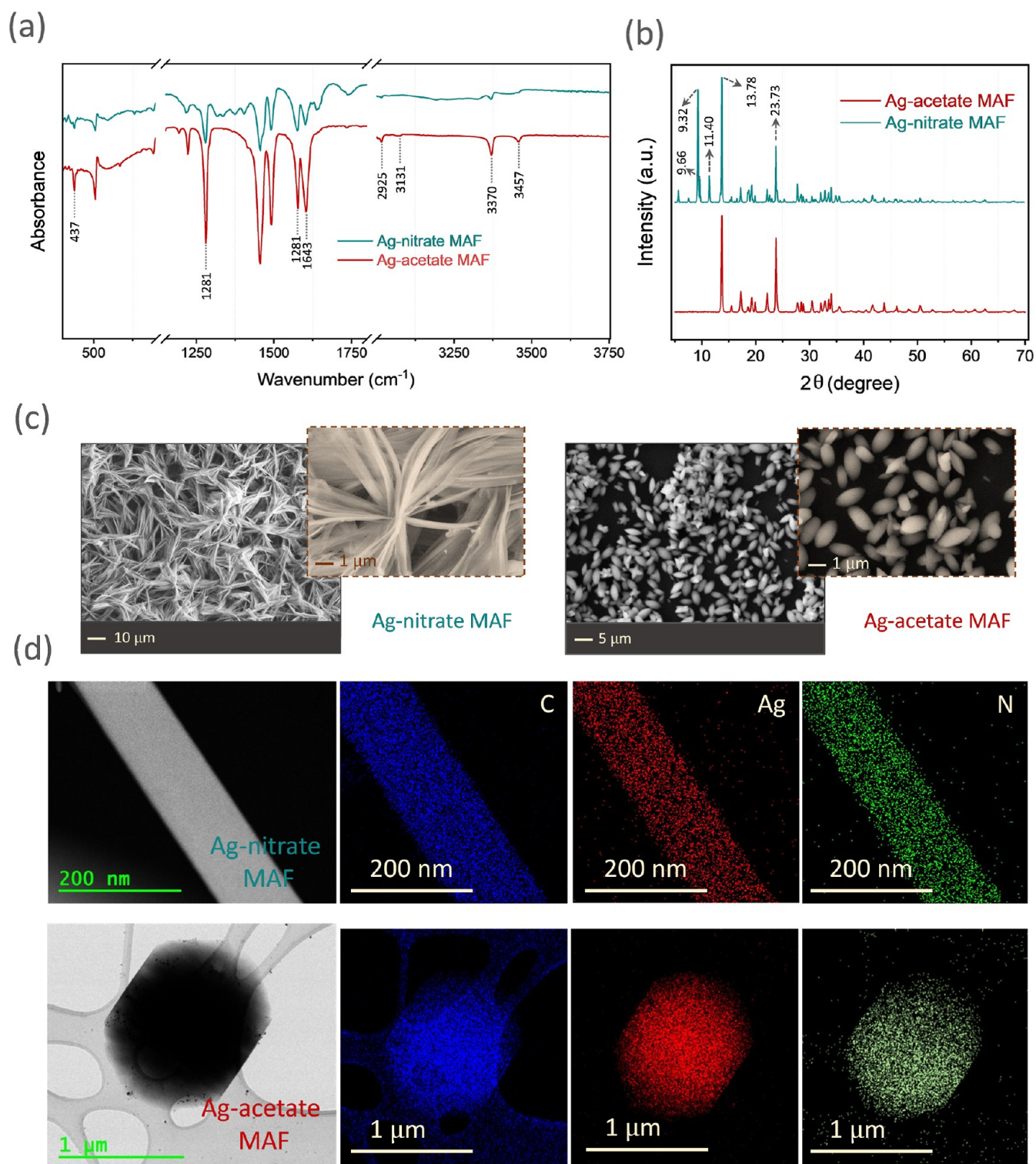


**Figure 2.** (a) FTIR spectra, (b) PXRD spectra, (c) SEM images, and (d) the SEM and TEM images and EDX mapping of Ag, C, and N atoms of Ag-nitrate MAF and Ag-acetate MAF. The TEM images show the nanoribbon for the Ag-nit-MAF and hexagonal structures for the Ag-acetate MAF.

the biofouling experiments, one vial containing 1 mL of the cryopreserved cells was gently thawed in a 37 °C water bath for 15 min and then added to a sterile flask containing 50 mL of LB (Luria–Bertani) media. The inoculated flask was placed in an incubator to maintain (37 °C) and shaken at 200 rpm (rpm) until an optical density of 1.5 at 600 nm (measured using an 800 TS absorbance reader) was achieved. This expanded cell stock was subsequently utilized to inoculate a larger volume of 1 L of

LB media, which was grown in the same incubator under the same conditions for several more hours to the same optical density (corresponding to mid log-phase). The 1 L culture was then centrifuged at 4000 rpm for 2 min, and the resulting cell pellet was gently washed three times with sterile phosphate-buffered saline (PBS, 10 mM, pH 7) to remove any residual LB medium. The bacteria were resuspended in 50 mL of PBS, yielding a stock solution with a cell concentration of 107 colony-

forming units (cfu)/mL, which was used for subsequent antibacterial and antifouling assessments.

**3.4.2. Bacterial Adhesion and Viability.** To examine cell morphology, the RO membrane samples were analyzed using SEM after bacterial contact.<sup>39</sup> A 3.5 cm<sup>2</sup> membrane sample was placed in a 6-well plastic plate with the active layer facing the bacterial suspension. Log-phase bacterial suspensions (with a concentration of 10<sup>7</sup> cfu/mL) were applied to the membrane's active layer and incubated at 37 °C. The excess solution was removed after 1 h. The membrane samples were then gently rinsed with sterile PBS and then fixed with a 2% glutaraldehyde solution at ambient temperature for 2 h. Following fixation, the samples underwent a graded ethanol dehydration process, transitioning from 50% to 100% ethanol, in preparation for field emission scanning electron microscopy (FESEM) analysis. Finally, the samples were desiccated using nitrogen gas to remove any remaining moisture.

**3.4.3. Antibacterial Activity Assessment of the Membranes.** Viability staining was performed to differentiate between live and dead bacteria on the membrane surfaces. SYTO 9-stained cells (green) indicated live bacteria, while PI-stained cells (red) represented dead bacteria. Confocal laser scanning microscopy (CLSM, Olympus) combined with fluorescence imaging was used to capture live/dead bacterial images. Fluorescence images were recorded using a Leica DMRXE microscope with a 100× PlanApo objective lens, coupled to a Tucsens TC-3 digital image capture system, and processed using TS View software (On Focus Laboratories, ver. 7). The PI and SYTO 9 molecules were excited by the light source, and their corresponding red and green fluorescence emissions were detected through filter cubes. SYTO 9 was excited at 450–490 nm with an emission wavelength >515 nm, while PI was excited at 515–560 nm with an emission wavelength >590 nm. For each imaging experiment, 1.0 mL of bacterial stock suspension (10<sup>7</sup> cfu/mL) was applied to a 1 cm<sup>2</sup> membrane surface. After 1 h of incubation, excess bacterial pellets were rinsed off with a 10 mM PBS solution. The samples were then stained with SYTO 9 (20 μM for 15–20 min in darkness at ambient temperature) and PI (5 μM for 5–10 min in darkness). The stained membranes were covered with glass coverslips and placed on the microscope stage after washing away any residual stain with PBS. Fifteen fluorescence images were captured for each membrane, with over 2000 cells counted in three separate experiments. The live and dead cell counts were used to calculate the percentage of live bacteria on each membrane surface. At least two membrane samples were analyzed for each test, and the average results from three trials were reported for both the pristine TFC and Ag-MAFs-functionalized membranes.

**3.5. Dynamic Organic and Biofouling Experiments.** The fouling resistance of the pristine and Ag-MAFs functionalized membranes was evaluated by dynamic fouling experiments using a lab-scale cross-flow RO filtration setup. Each membrane was tested with 100 ppm foulant solution for 8 h at room temperature. Bovine serum albumin (BSA, 100 mg/L) was used as a model organic foulant to simulate polysaccharide and protein fouling, respectively.<sup>32</sup> A transmembrane pressure of 150 psi at a flow rate of 4.5 L·min<sup>-1</sup> was applied for fouling tests. For the biofouling experiments, *E. coli* bacteria (10<sup>7</sup> cfu/mL) were introduced into the feed solution (along with 500 ppm of LB in 100 mM of PBS) to simulate biofouling on the membrane surface, following the same conditions used for organic fouling. Prior to each biofouling test, the system was thoroughly cleaned and disinfected using deionized water and 70 wt % ethanol

solution for 1 h to eliminate any potential bacterial interference. After disinfection, the RO system was rinsed three times with deionized water to ensure the complete removal of cleaning agents. The log-phase *E. coli* culture, with an optical density of 0.35 ± 0.2 at 600 nm (OD<sub>600</sub>),<sup>39</sup> was added to the feed solution (LB broth at 100 mg/L in 10 mM PBS) by inoculating with 50 mL of bacterial culture, achieving an initial concentration of 10<sup>7</sup> cfu/mL.

The flux decline ratio was calculated using the following equation

$$FD = \frac{J_f - J_i}{J_i} \times 100 \quad (3)$$

where  $J_f$  and  $J_i$  represent the final and initial water flux in fouling experiments. After each fouling experiment, the membranes were washed using deionized water for 30 min. After cleaning, the water flux was recorded to assess the flux recovery ratio.

$$FRR = \frac{J_{\text{recovered}}}{J_i} \times 100 \quad (4)$$

where  $J_{\text{recovered}}$  is the water flux after the cleaning process.

## 4. RESULTS AND DISCUSSION

**4.1. Chemical and Morphological Characterizations of the Synthesized Ag-MAFs.** FTIR analysis was conducted to verify the chemical structure of Ag-MAFs and the coordination between silver and the amino benzimidazole linker. Figure 2a shows the FTIR spectra of Ag-nitrate and Ag-acetate MAFs, which display the characteristic peaks of the Ag-amino benzimidazole structure. The absorption peaks at 3131, 2925, 1643, and 1575 cm<sup>-1</sup> correspond to the aromatic C–H stretching, aliphatic C–H stretching, aromatic C=C stretching, and C=N stretching vibrations, respectively.<sup>40</sup> The peak at 1281 cm<sup>-1</sup> can be assigned to the C–N stretching vibration of benzimidazole.<sup>41</sup> The symmetric and asymmetric –NH<sub>2</sub> stretching vibrations appeared in the range of 3340–3420 cm<sup>-1</sup> and 342–3500 cm<sup>-1</sup>, respectively.<sup>42</sup> In this study, the absorption peaks appeared at 3370 and 3457 cm<sup>-1</sup>, corresponding to –NH<sub>2</sub> of 2-aminobenzimidazole.<sup>43</sup> The peak observed at 437 cm<sup>-1</sup> can be attributed to the linkage between metal (Ag) and the imidazole ligand.<sup>44</sup>

Figure 2b illustrates the PXRD spectra of Ag-MAFs. The unit cells and the 19 identified peaks for each sample, along with their corresponding Miller indices, were detected by the TREOR90 algorithm. The crystalline structures of the MAFs synthesized using Ag acetate and Ag nitrate salts are classified as monoclinic and triclinic crystals based on the Bravais lattice classification.<sup>45</sup> Particularly, four characteristic peaks were identified for the Ag-acetate MAF, with the most intense one at 13.78° attributed to the (200) crystal plane of the monoclinic structure. Similarly, five characteristic peaks were observed for the Ag-nitrate MAF at 9.32°, 9.66°, 11.40°, 13.76°, and 23.73°, corresponding to the (010), (100), (002), (–1 –1 1), and (12) crystal planes, respectively, which belong to its triclinic structure. While the PXRD patterns of both samples display well-formed crystalline planes and the intensity of the sharpest peaks demonstrates almost the same crystallinity, the patterns reveal a shift in the crystalline phase with the appearance of new peaks as the type of salt was altered in the synthesis method. The type of metal salt and its reaction rate with the amino-benzimidazole determine the crystalline structure.

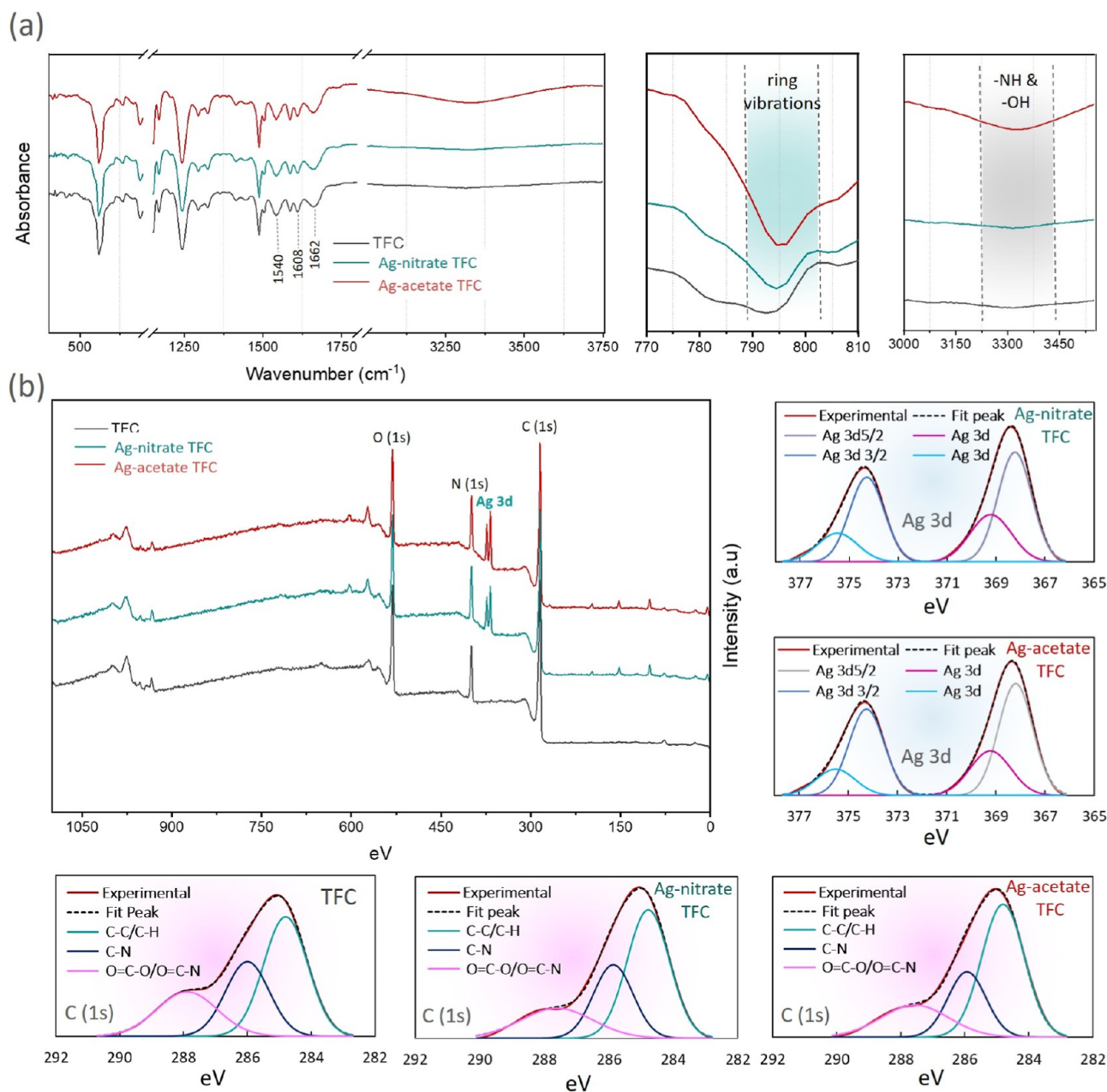


**Figure 3.** (a) FTIR spectra of the pristine TFC and Ag-MAFs surface functionalized membranes, and (b) general XPS survey and carbon/silver high-resolution XPS spectra of pristine TFC and Ag-MAFs functionalized membranes.

Figure 2c,d reveal the SEM and TEM images of the synthesized Ag-MAFs. Ag-nitrate MAFs form nanoribbons with an average diameter of 100–200 nm. Ag-acetate MAFs have hexagonal structures with an average particle size of less than 1  $\mu\text{m}$ . EDX mapping of Ag-MAFs confirms the presence of carbon (C), nitrogen (N), and silver (Ag) atoms (Figure 2d). Additionally, the EDX mapping of Ag-MAFs indicates that both MAFs have a homogeneous distribution of C, N, and Ag atoms throughout their entire frameworks.

The difference in structural formation between Ag-acetate MAF (hexagonal) and Ag-nitrate MAF (nanoribbons) can be attributed to the different coordination chemistry of silver acetate and silver nitrate, ion pairing tendencies, and the role of the counterions in the crystal assembly.<sup>46</sup> The acetate anion ( $\text{CH}_3\text{COO}^-$ ) is a weaker and more flexible ligand than nitrate.<sup>47,48</sup> This allows for more efficient coordination between

the  $\text{Ag}^+$  ion and the benzimidazole linker, resulting in a well-ordered, stable hexagonal lattice structure. Silver nitrate, on the other hand, has a stronger coordination interaction between  $\text{Ag}^+$  and the nitrate anion ( $\text{NO}_3^-$ ), making the silver ion less readily available for coordination with the benzimidazole linker.<sup>47</sup> This results in the formation of nanoribbons in Ag-nitrate MAFs, as the silver ions form linear chains along with the benzimidazole linkers. These 1D chains, when linked together through intermolecular forces like hydrogen bonding and  $\pi$ - $\pi$  interactions, assemble into 2D nanoribbons.<sup>49</sup> The resulting nanoribbons have more elongated, less tightly packed structures than the hexagonal arrays formed by Ag-acetate.

**4.2. Chemical Bonding of Ag-MAFs to the Membrane Surface.** The FTIR spectra of the pristine TFC and Ag-MAFs functionalized membranes are presented in Figure 3a. Characteristic peaks of the polyamide layer, formed through

**Table 1. Elemental Compositions, O/N Ratio, and C 1s Species of the Pristine TFC and Ag-MAFs Functionalized Membranes**

membrane	atomic concentration (%)				O/N ratio	C 1s species		
	C (1s)	O (1s)	N (1s)	Ag (3d)		C=C/C-H	C-N	O=C-O/O=C-N
TFC	73.87	15.27	10.86	0.00	1.40	51.20	26.90	21.90
Ag-nitrate TFC	73.81	14.25	10.49	1.46	1.35	51.70	27.60	20.70
Ag-acetate TFC	72.85	13.20	12.22	1.73	1.08	51.30	28.20	20.40

IP reaction, were observed at  $1662\text{ cm}^{-1}$  (C=O stretching vibrations of amide I),  $1540\text{ cm}^{-1}$  (in-plane N-H bending and C-N stretching vibrations of amide II), and  $1608\text{ cm}^{-1}$  (N-H stretching of amide) for all membranes.<sup>50</sup> After in situ functionalization of TFC membranes with Ag-MAFs, the intensity of peaks around  $770\text{--}790\text{ cm}^{-1}$  increased, likely due to overlap with the imidazole ring vibrations.<sup>51</sup> The characteristic peak for  $\text{-NH}_2$  stretching vibrations was detected at  $3300\text{--}3500\text{ cm}^{-1}$ , corresponding to the free amine group of 2-benzimidazole.<sup>43</sup> Notably, the intensity of peaks around  $3000\text{--}3500\text{ cm}^{-1}$  for Ag-MAFs is higher than that of the pristine TFC. This increase is likely due to the overlap of the amine group adsorption band from the Ag-MAFs and remaining carboxylic groups on the membrane surface.

XPS measurements were performed to assess the elemental composition and functional groups of the pristine TFC and Ag-MAFs functionalized membranes. Figure 3b shows the general survey and high resolution spectra of carbon and silver peaks. The energy peaks of the pristine TFC membrane are associated with carbon (C), oxygen (O), and nitrogen (N), located at 284.8, 399, and 532 eV, respectively.<sup>52</sup> However, two new peaks for silver (Ag  $3d_{5/2}$  at 368.2 eV and Ag  $3d_{3/2}$  at 374.2 eV) appeared in the spectra of the Ag-MAFs functionalized TFC membranes, confirming the presence of Ag-MAFs nanoparticles on the membrane surface. Table 1 summarizes the elemental compositions and O/N ratio of all membranes. Following Ag-MAFs functionalization, the O/N ratio decreased due to an increase in nitrogen content (resulting from the 2-amino-benzimidazole ligand) and the loss of OH groups from the surface. In addition, the Ag-acetate TFC exhibited a higher Ag content than Ag-nitrate TFC, suggesting more Ag-MAFs were formed. This observation is further supported by TEM images of Ag-MAFs (Figure 2), where Ag-acetate MAF showed a higher density of Ag atoms than Ag-nitrate MAF.

Detailed insights into the chemical bonding of the active layer can be derived through the deconvolution of high-resolution C 1s, N 1s, and O 1s spectra, as illustrated in Figure 3b. The high-resolution C 1s spectra of the TFC membrane reveal three distinct peaks at 284.8 eV (C-C or C-H bonds),<sup>53</sup> 286 eV (attributed to C-N bonds), and 288 eV (O=C-O and amide O=C-N bonds).<sup>54</sup> The increased intensity of the C-N peak in the Ag-MAF TFC membranes suggests the presence of free  $\text{-NH}_2$  groups from the amino-benzimidazole ligand in Ag-MAFs.<sup>55</sup> Furthermore, the lower O=C-O/O=C-N ratio in Ag-MAF TFC membranes compared to the pristine TFC membrane can be attributed to a reduction in carboxylic groups on the membrane surface after functionalization. The deconvoluted Ag spectrum of the Ag-MAFs membrane revealed Ag 3d peaks at 368.2, 369.2, 374.2, and 375.5 eV, accompanied by characteristic Ag  $3d_{5/2}$  and Ag  $3d_{3/2}$  peaks at 368.2 and 374.2 eV, respectively.<sup>56</sup>

**4.3. Morphological Assessment of the Pristine and Ag-MAFs TFC Membranes.** Figure 4 shows the surface and cross-section morphology of TFC and Ag-MAFs TFC membranes. Figure 4a represents the top surface SEM of the pristine TFC

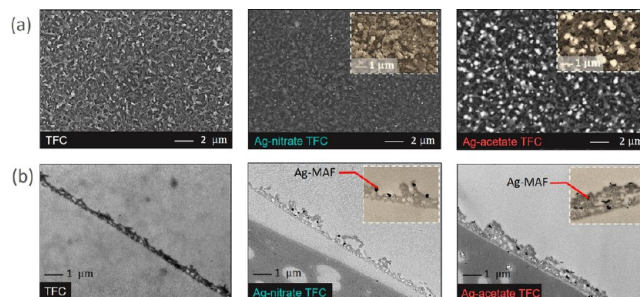


**Figure 4.** (a) Top surface SEM images of the pristine TFC and Ag-MAFs functionalized TFC membranes, and (b) cross-section TEM images of the pristine TFC and Ag-MAFs functionalized TFC membranes. The bright spots in SEM images and dark spots in TEM images represent Ag-MAFs nanoparticles on the membrane surface.

and Ag-MAFs TFC membranes at different magnifications. The pristine TFC membrane has a uniform ridge-and-valley structure typical of the cross-linked fully aromatic polyamide prepared through IP reaction.<sup>31,57</sup> However, some bright spots formed on the surface of the Ag-nitrate TFC membrane, indicating the uniform formation of Ag-nitrate MAF nanoparticles over the entire membrane surface without aggregation. Table 2 shows that the EDX elemental composition of Ag-

**Table 2. Energy-Dispersive X-ray (EDX) Results: Elemental Compositions of the Pristine TFC and Ag-MAFs Functionalized Membranes**

membrane	atomic composition (%)					
	C	O	N	Ag	S	Cl
TFC	78.45	11.39	2.91		5.67	1.58
Ag-nitrate TFC	83.74	7.97	1.73	1.14	5.75	0.08
Ag-acetate TFC	82.22	7.17	0.55	3.80	6.23	1.03

nitrate TFC confirms the presence of Ag atoms. The same morphology was observed for the Ag-acetate TFC membrane, featuring numerous Ag-MAFs on the surface. The cross-sectional TEM images (Figure 4b) of the functionalized membrane provide further insights into the structure and Ag-MAFs nanoparticle dispersion. The Ag-MAFs nanoparticles appear as dark spots. Consistent with the SEM analysis, the Ag-MAFs are uniformly distributed across the entire TFC membrane surface. Notably, the cross-sectional TEM image reveals that Ag-MAFs are present both on the TFC surface, suggesting the successful formation of Ag-MAFs on the active sites. Due to the high reactivity of Ag ions with the amino-benzimidazole linker, the ion mobility increases, facilitating the formation of Ag-MAFs after the deposition of Ag ions. When Ag ions are nucleated on the surface, secondary growth occurs. This secondary evolution toward crystal saturation ultimately improves the stability of the modification by reducing Ag-MAFs leaching. Finally, despite the formation of numerous Ag-MAFs nanoparticles on the membrane surfaces, the overall

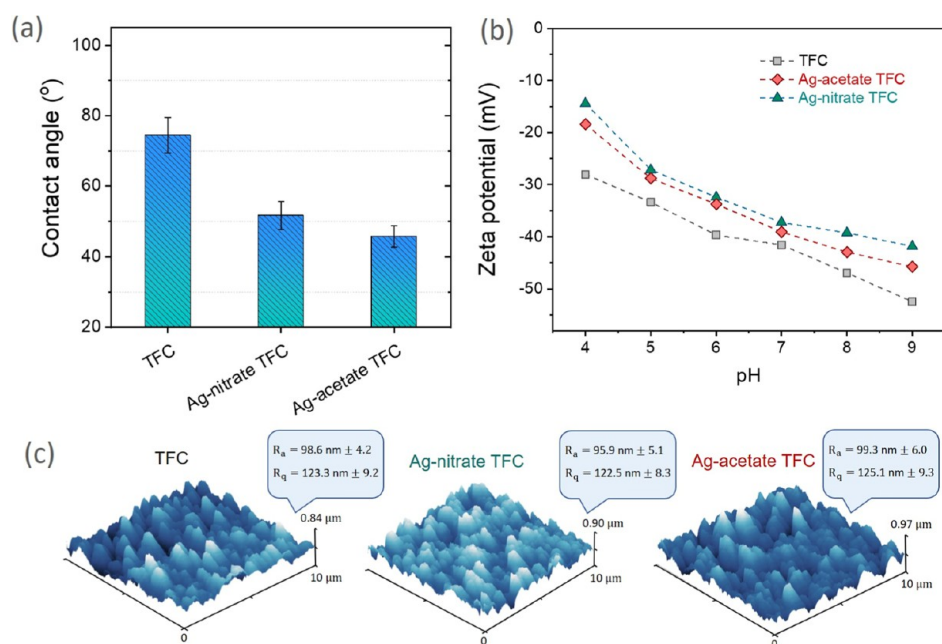


**Figure 5.** (a) Contact angle, (b) zeta potential, and (c) 3D AFM images and AFM roughness parameters of the pristine TFC and in-situ deposited Ag-MAFs TFC membranes.

ridge-and-valley morphology of the TFC membranes was largely retained. This observation suggests that the Ag-MAFs nanoparticles are deposited in a discontinuous pattern on the surface rather than forming a continuous coating layer.

The observed morphological differences between Ag-MAFs synthesized in bulk and those grown in situ on thin-film composite (TFC) membranes can be attributed to distinct nucleation and growth mechanisms influenced by the presence of the membrane substrate. In a homogeneous solution, MAFs nucleate and grow without spatial constraints, allowing the formation of well-defined structures such as nanoribbons or hexagonal crystals. The absence of a substrate facilitates unrestricted crystal nucleation and growth, resulting in uniform and characteristic morphologies. Typically conducted under controlled conditions with uniform concentration and solvent environment, bulk synthesis promotes the growth of well-ordered crystals. Studies have shown that the crystallization of MOFs is highly sensitive to the conditions under which nucleation and growth occur. The interaction between MOF precursors and a substrate can lead to the formation of thin films with controlled orientation and morphology, which are often distinct from their bulk counterparts.<sup>58</sup>

Comparing modified membranes, more Ag-MAFs formed on the Ag-acetate TFC surface. The higher quantities of the Ag-acetate MAFs can be ascribed to their faster nucleation rate during the deposition process and the more rapid coordination degree during Ag-acetate MAFs formation and growth. This feature was confirmed by the EDX spectra of the Ag-MAFs membranes (Table 2), where the Ag-acetate MAF TFC showed a higher Ag content than the Ag-nitrate TFC.

**4.4. The Wettability, Surface Charge, and Surface Roughness of the Synthesized Membranes.** Figure 5a illustrates the water contact angle of pristine TFC and Ag-MAFs-modified membranes. The contact angle was reduced from 74.5° to 51.7° and 45.8° for pristine TFC, Ag-nitrate TFC, and Ag-acetate TFC, respectively. The increase in surface hydrophilicity of Ag-MAFs-modified TFC membranes origi-

nates from the presence of amine functional groups of Ag-MAFs. Hydrophilic behavior can be further enhanced by the presence of additional sites for hydrogen bonding. Therefore, the increased surface combined with the hydrophilic nature of the amine groups leads to a significant improvement in surface hydrophilicity, promoting better water interaction. Membranes with a hydrophilic surface facilitate the attraction of water molecules via interfacial electrostatic forces, reducing foulant attachment and improving antifouling propensity.<sup>6,59,60</sup>

The surface charge of the membranes was measured by zeta potential over the pH range of 4–9 (Figure 5b). The carboxylic groups of the pristine TFC membrane deprotonate as the pH rises beyond their  $pK_a$ , resulting in a highly negatively charged surface.<sup>61</sup> However, the Ag-MAFs-modified membranes have less negative surface charge due to the presence of amine functional groups (amino-benzimidazole ligand). The TFC membrane shows a negative charge when its surface is covered with the carboxylic groups, but this negative charge is reduced when those groups are replaced with the amine-containing Ag-MAFs. The amine groups within the amino-benzimidazole ligand are basic and will readily accept protons from the surrounding environment, especially in neutral or acidic conditions. When the amine groups are exposed to low pH, they become protonated, forming  $-\text{NH}_3^+$ . The protonated amine groups carry a positive charge, which contributes to a net positive charge on the surface of the membrane. The combined effect of amines in both the ligand and the structure of the TFC membrane further shifts the surface potential toward the positive direction for the Ag-MAFs-modified membranes.

Figure 5c shows the 3D AFM images and roughness parameters,  $R_a$  (average roughness) and  $R_q$  (root-mean-squared roughness), of TFC and Ag-MAFs modified TFCs. The roughness parameters of Ag-nitrate TFC decreased slightly upon surface modification, whereas those of the Ag-acetate-modified TFC membrane exhibited a slight increase compared to the pristine TFC membrane. The slight decrease in surface roughness observed in the Ag-nitrate TFC membrane may be

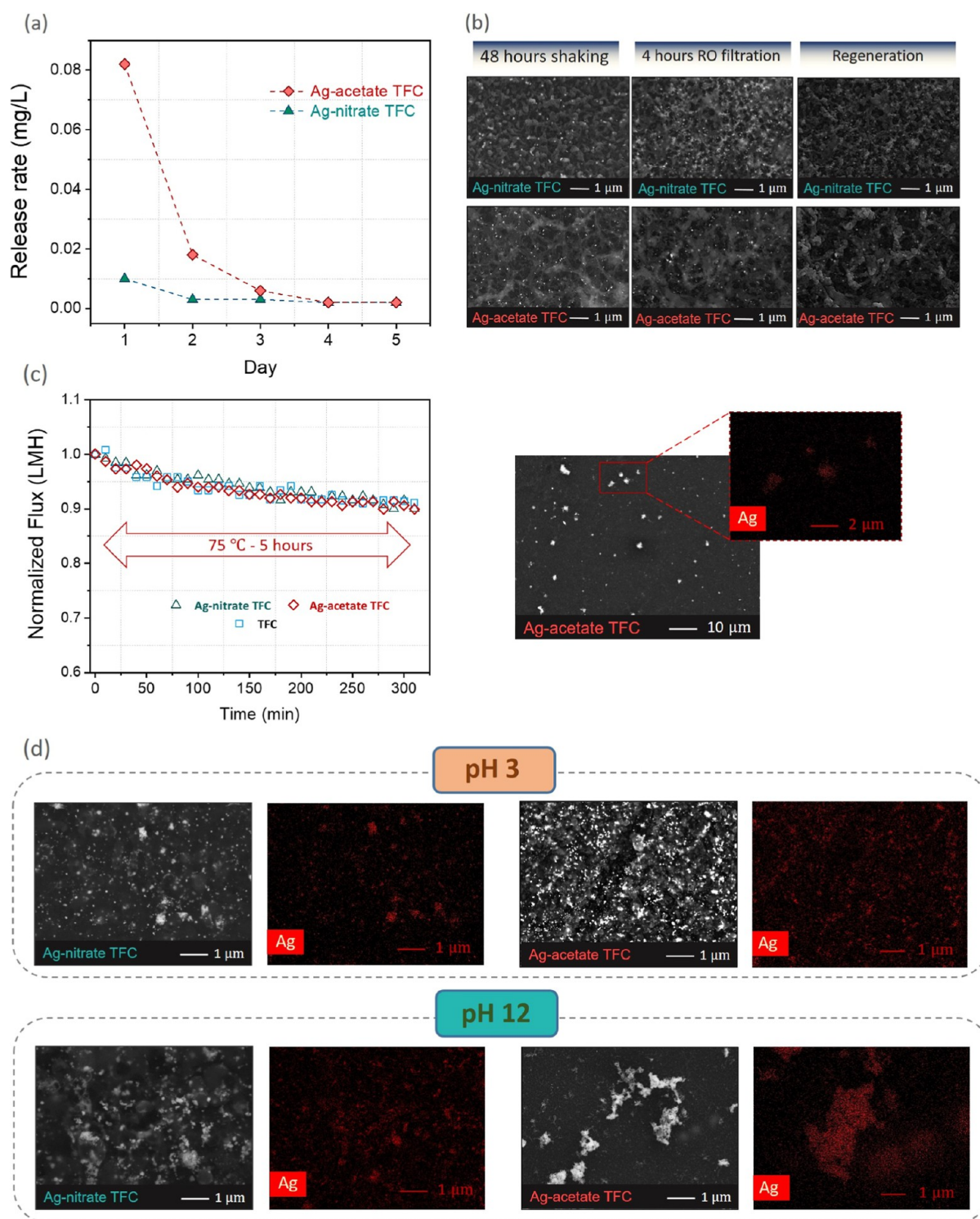


**Figure 6.** (a) The release rate of Ag ions for the Ag-MAFs TFC membranes, (b) the SEM images of Ag-MAFs TFC membranes after 48 h of shaking, 4 h RO testing, and regeneration, (c) the thermal stability of the neat TFC and Ag-MAFs membranes over high-temperature RO process conducted at 75 °C using 2 g/L NaCl as feed solution; the SEM images of Ag-acetate MAFs TFC membranes after 12 h RO testing, and (d) the SEM images of Ag-MAFs membranes after exposure to aqueous solutions at pH 3 and pH 12 for 7 days at room temperature.

attributed to the formation of relatively small Ag-MAFs nanoparticles, which likely smooth the surface by filling minor irregularities. Conversely, the slight roughness increase in the Ag-acetate TFC membrane could be due to localized nanoparticle aggregation, leading to a more pronounced surface texture. Although the changes are statistically distinguishable, these variations were marginal, indicating that surface

modification and deposition behavior can induce subtle nuances in topography. In other words, the intrinsic ridge and valley morphology of the TFC membrane remained largely unchanged after Ag-acetate MAFs deposition, attributed to the small sizes of the Ag-MAFs nanoparticles formed on the membrane surface.<sup>62</sup>

**4.5. Stability and Regeneration of Ag-MAFs on the Membrane Surface.** The stability of the surface functionalized

membranes can be determined by the release rate of Ag-MAFs nanoparticles from the surface. The release rate of silver ions from the membranes was measured over 5 days by immersing the Ag-MAFs-modified membranes in water. As illustrated in Figure 6, the Ag-acetate MAF membrane exhibited a higher release rate in the first 2 days compared to the Ag-nitrate MAF membrane. A higher degree of surface functionalization of Ag-acetate MAF nanostructures ensured greater quantities and more uniform coverage on the active sites of the membrane surface. The initial leaching phase involved some loss of unattached Ag-MAFs from the surface. After the second day, the release rate for both membranes significantly decreased, stabilizing at a negligible level by the third day, indicating minimal long-term leaching.<sup>63</sup>

Figure 6b shows the SEM images of the top surface of Ag-MAFs TFC membranes after 48 h of shaking, 4 h of RO testing, and regeneration. The bright spots present on the surface are indicative of Ag-MAFs. Despite a decrease in the number of Ag-MAFs nanoparticles, more of them still remained on the surface after RO filtration and shaking. This observation validates the strong interactions of the Ag-MAFs with the surface.

The replenishment of Ag-MAFs nanoparticles after release is a promising technique for maintaining the antibacterial activity of the membrane surface over the long-term.<sup>64</sup> In this study, the membranes were initially immersed in water for 20 days, then tested using the RO process, and subsequently regenerated using the same initial surface deposition method after depletion, employing water and ethanol as solvents with minimal impact on membrane properties. Unlike harsh solvents, they preserve the polyamide layer and rejection performance, ensuring sustainable regeneration. This process maintains the membrane's structural integrity and functionalization, preserving its antifouling, antibacterial properties, and desalination efficiency.

However, it should be noted that the formation of Ag-MAFs on the depleted surface is different from the initial deposition. Even though some Ag-MAFs might deposit on the freshly formed carboxyl groups, the number of MAFs were lower than the initial MAFs formation. Moreover, due to incomplete release and different chemical surface properties, some Ag-MAFs were still present on the surface and inhibited achieving the same deposition degree.<sup>65</sup> The previously deposited Ag-MAFs reached a level of saturation that hinders proper nucleation of Ag ions and secondary growth at the reactive sites, thereby altering the initial regeneration process.

To further evaluate the robustness of Ag-MAFs-modified membranes, we conducted high-temperature stability tests at 75 °C. The high-temperature flux and rejection of the membranes were assessed by increasing the operating temperature from 25 to 75 °C, followed by continuous flux monitoring over 7 h. The results indicated that membrane performance, in terms of water flux and salt rejection, remained unaffected. The salt rejection of the neat TFC, Ag-nit-MAFs, and Ag-act-MAFs membranes remained stable even after 7 h of continuous high-temperature RO testing, attaining rejection of 97.17%, 97.54%, and 97.10%, respectively. As illustrated in Figure 6c, the results show that water flux increased with temperature for all membranes. However, the neat TFC membrane exhibited the lowest flux, while both Ag-MAFs-functionalized membranes demonstrated improved flux at 75 °C without sacrificing the salt rejection. Although there were slight differences in flux between the two Ag-MAFs-modified membranes, the Ag-nit-MAFs membrane exhibited a more pronounced decline in flux compared to the Ag-act-MAFs membrane. This suggests that the Ag-act-MAFs

membrane possesses greater thermal stability, likely due to the higher density of Ag-act-MAFs on the surface, which acts as a thermal barrier against high-temperature feedwater. Overall, all of these observations demonstrate the long-lasting and durable binding of Ag-MAFs to the TFC surface.

Similarly, the figure depicts the SEM image and the relevant EDX spectrum of the Ag-acetate MAFs-functionalized membranes after a 12 h RO test (Figure 6c). It is worth mentioning that Ag-MAFs are only attached to the active sites of the membrane surface and form nanoparticle structures. Furthermore, due to the covalent binding, Ag-MAFs still remained attached to the membrane surface even after a 12 h RO filtration test. Despite showing slight changes, the binding between Ag-MAFs and the membrane surface is not affected by the cross-flow filtration. Because the RO is a high-pressure driven process, the hydrodynamic conditions near the membrane surface exert a strong influence on the Ag-MAFs release rate and the possibility of rapid silver leakage unless the binding is of a covalent type. Additionally, the EDX mapping of Ag-MAFs functionalized TFC membrane clearly validates the existence of silver on the structure of Ag-MAFs nanoparticles and hence the membrane surface (after 12 h RO test).

To assess pH stability, we soaked Ag-MAFs-modified membranes at pH 3 and pH 12 for 7 days, followed by SEM imaging and EDX mapping to examine potential structural or compositional changes. The SEM imaging, along with the corresponding EDX mapping, proves that Ag-MAFs are present on the surface even when tested at harsh acid/basic conditions for 7 days (Figure 6d).

**4.6. Antibacterial Activity of Ag-MAFs-Modified TFC Membranes.** To evaluate the antibacterial activity of the membranes, bacterial cell membrane integrity was visualized using SEM imaging. Figure 7a illustrates a clear distinction

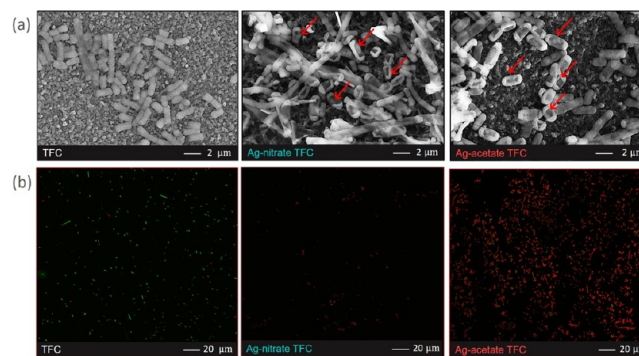


**Figure 7.** Antibacterial activity of pristine TFC and Ag-MAFs modified membranes against *E. coli* bacteria: (a) SEM images of *E. coli* cells on TFC, Ag-nitrate TFC, and Ag-acetate TFC membranes, respectively; (b) confocal images stained with SYTO 9 and PI showing live (green) and dead (red) bacteria on TFC, Ag-nitrate TFC, and Ag-acetate TFC membranes.

between live and dead *E. coli* cells. Bacteria in contact with the pristine TFC membrane retained their original structure, exhibiting almost no physical disruption. However, *E. coli* attached to the surface-modified membranes displayed significant morphological defects in the cell shape, including flattened or shrunken cells. This antibacterial effect of Ag-MAFs nanoparticles can be attributed to the interaction of Ag<sup>+</sup> with nitrogen, oxygen, or sulfur-containing functional groups of bacterial deoxyribonucleic acid (DNA), bacterial proteins, or

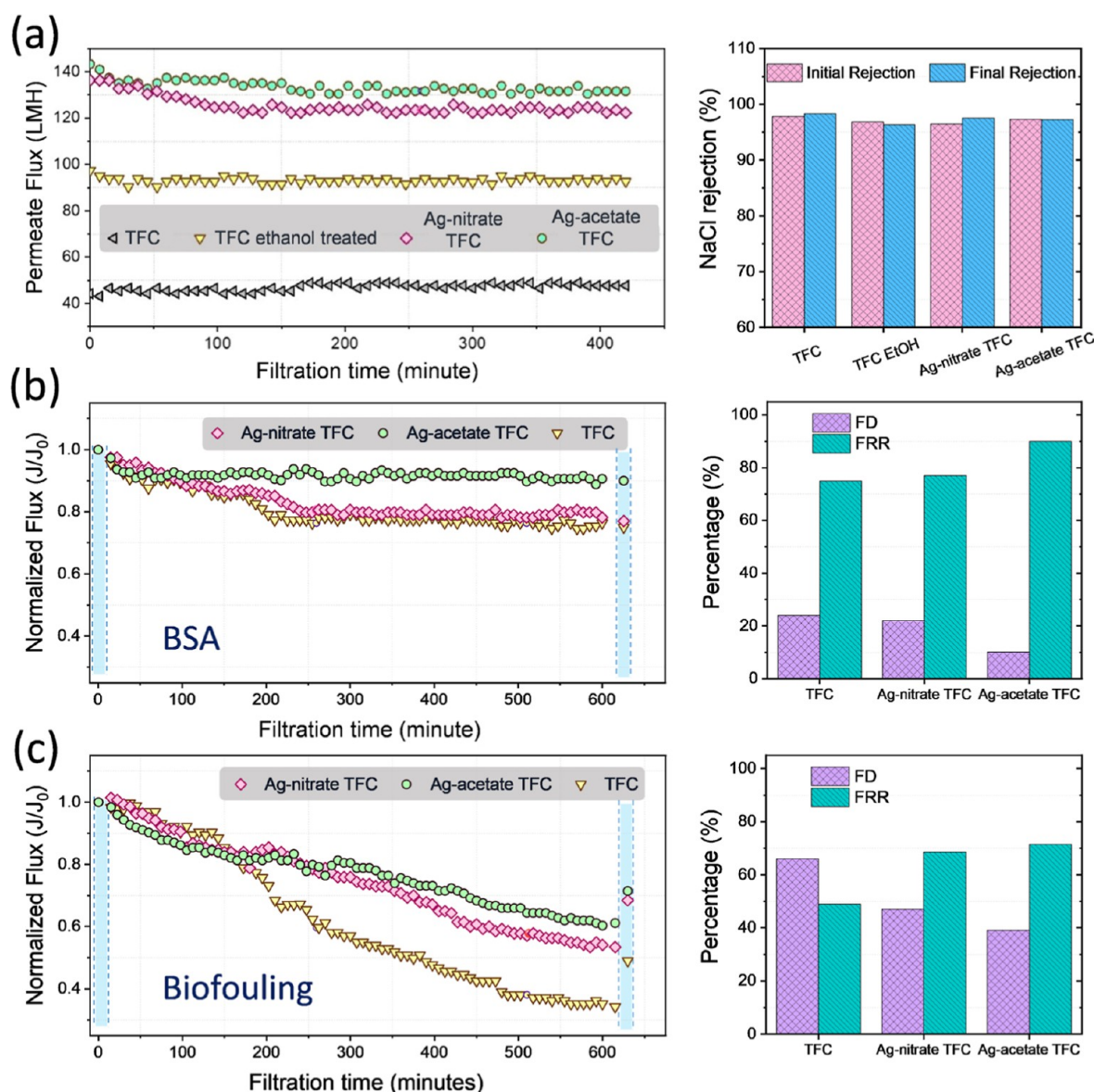


**Figure 8.** (a) Permeate water flux and NaCl rejection of the pristine TFC and Ag-MAFs membranes and normalized water flux versus filtration time of the pristine TFC and Ag-MAFs functionalized membranes during (b) BSA, and (c) LB broth of 500 mg/L & PBS of 100 mM as feed solution for *E. coli*.

bacterial lipids, deactivating bacterial cells.<sup>66</sup> Meanwhile, Ag ions exert charge stress on the bacterial cell membrane, leading to subsequent deformation. When Ag ions infiltrate the cell wall, they disrupt the integrity and shape of the cytoplasmic membrane, causing leakage of intracellular substances and leading to cell death.<sup>67</sup> Moreover, the angular morphology and small crystal size of Ag-MAFs enhance their biocidal efficacy, providing better contact with bacterial cells. Smaller Ag nanoparticles, with their higher surface-area-to-volume ratio, generate more reactive oxygen species (ROS), damaging essential biomolecules such as DNA, proteins, and lipids, contributing to cell death.<sup>68</sup>

Confocal imaging (Figure 7b) of live/dead bacteria further confirmed the antibacterial performance of the Ag-MAFs membranes. While a high number of live *E. coli* (green) adhered to the TFC surface, both Ag-MAFs functionalized membranes exhibited a bacterial mortality rate of approximately 99%. This enhanced antibacterial activity aligns with the observed SEM

results, indicating the effective disruption of bacterial cell integrity.

The enhanced antibacterial activity of Ag-MAFs-functionalized membranes stems from the controlled release of both amino-benzimidazole linkers and Ag<sup>+</sup> ions, which act as a reservoir for prolonged antibacterial effects via direct contact and sustained ion release.<sup>20</sup> In the MAF framework, Ag ions are chemically bonded to organic ligands, ensuring stable integration that prevents rapid dissolution while allowing a steady release of Ag<sup>+</sup> ions.<sup>69</sup> The porous structure of Ag-MAFs enables uniform distribution of Ag sites, facilitating continuous ion release from the membrane surface. This dual mechanism, i.e., contact-based and ion-release-based, ensures effective antibacterial action.<sup>69,70</sup> The antibacterial properties of Ag<sup>+</sup> ions arise from several mechanisms:

- (1) Protein and Nucleic Acid Interference: The positive charge of Ag ions leads them to bind strongly to negatively charged oxygen, nitrogen- and sulfur-containing proteins on cell membranes, as well as to biomolecules like nucleic

acids, disrupting essential functions such as cell division and respiration, ultimately causing bacterial death.

- (2) Lipid Membrane Disruption: Ag ions increase cytoplasmic membrane permeability, leading to structural disruption of the bacterial cell membrane.
- (3) Enzyme Inactivation and ROS Generation: Penetrated Ag ions inactivate key enzymes and promote the formation of ROS, further damaging cell membranes and interfering with DNA replication.<sup>71</sup>

Furthermore, the release of the benzimidazole linker in Ag-MAFs may alter the charge distribution on the bacterial membrane, contributing to a synergistic antibacterial effect.<sup>69,72</sup> Benzimidazole-based compounds, such as those present in Ag-MAFs, have demonstrated antibacterial properties against both Gram-negative and Gram-positive bacteria.<sup>73</sup> Indeed, several benzimidazole-containing compounds have been shown to exhibit good antibacterial activity against *E. coli*.<sup>74</sup> Benzimidazole disrupts glucose uptake, leading to reduced ATP generation. The structural similarity of benzimidazole to purine allows it to act as a bioisostere and a competitive inhibitor, interfering with the synthesis of nucleic acids (and subsequently protein synthesis) and thereby inhibiting bacterial growth.<sup>75</sup>

Finally, the amino group present in the amino-benzimidazole structure is commonly found in numerous clinical bacteriocidal drugs and plays a crucial role in forming hydrogen bonds, coordinating with metal ions, accepting protons, and undergoing quaternization. These interactions not only enhance the physicochemical properties of the target molecules but also facilitate beneficial interactions with various enzymes and receptors within biological systems.<sup>76</sup> Schiff bases ( $-C=N-$ ), a key structural component in many antibacterial agents, can modulate pharmacokinetic properties and enhance antibacterial activity.<sup>77</sup> Additionally, positively charged nanomaterials interact more with the negatively charged bacterial cell walls, potentially disrupting cell membranes. In this regard, nanoparticles with amine functional groups have been shown to impair the electron transport chain in bacterial cells, causing cell disruption.<sup>78</sup> This disruption is believed to result from generating ROS and the subsequent oxidative stress, which interferes with the electron transport chain's function.<sup>79</sup> Bacterial cell walls generally carry a negative charge within a pH range of 4–9, which strengthens the electrostatic interactions between their membranes and positively charged nanoparticles, leading to enhanced antibacterial effects.<sup>78,80</sup> This is further evidenced by the stable attachment of positively charged silver-modified compounds to bacterial cells.<sup>78,81</sup>

Overall, the Ag-MAFs functionalized membranes enhance antibacterial activity due to the synergistic effects of Ag<sup>+</sup> ions and amino-benzimidazole ligands.<sup>20,69,82</sup> The presence of two bacterial growth inhibitors, Ag ions and amino-benzimidazole linkers, intensifies the RO membrane's antibacterial properties, preventing bacterial adhesion and biofilm formation.<sup>83</sup>

**4.7. Separation Performance and Antifouling Properties of Synthesized Membranes.** Figure 8a shows the permeate water flux of membranes for 7 h. All membranes had almost stable water flux over the test period. The Ag-acetate TFC and Ag-nitrate TFC membranes exhibited significantly higher water fluxes of 133 and 139 LMH, respectively, compared to the pristine TFC (45 LMH) and ethanol-treated TFC (99 LMH) membranes. The increased flux in the ethanol-treated TFC membrane can be attributed to the swelling of the polyamide layer induced by ethanol.<sup>84</sup> Ethanol may also detach

short, unbonded polymer chains formed during interfacial polymerization, increasing the polymeric structure's free volume and facilitating water permeation.<sup>15</sup> The substantial increase in water flux observed in the Ag-MAFs membranes indicates that surface functionalization enhanced membrane hydrophilicity. The higher presence of Ag-MAFs on the surface of the Ag-acetate TFC membrane resulted in slightly greater water flux than the Ag-nitrate TFC membrane. The Ag-acetate TFC membrane, with its higher number of amine functional groups, exhibited enhanced hydrophilicity, further facilitating water molecule passage. Moreover, all membranes sustained NaCl rejection over the entire 7 h filtration period. While our membrane's NaCl rejection ( $\sim 97.6\%$ ) is lower than some commercial RO membranes, it achieves a significantly higher water flux (133–139 LMH) compared to conventional RO membranes (20–60 LMH).<sup>85</sup> This trade-off between permeability and salt rejection is expected in high-flux membrane design.<sup>86</sup> Given its superior productivity and antibacterial properties, our membrane is well-suited for brackish water treatment, wastewater reuse, and applications where high water flux is a priority.

The dynamic fouling behavior of pristine TFC and Ag-MAFs-functionalized membranes was evaluated using BSA and *E. coli*. Figure 8b,c shows the normalized water flux of these membranes over filtration time. As shown in Figure 8b, the normalized fluxes of all membranes decreased gradually after the addition of BSA. The pristine TFC membrane exhibited the greatest flux decline (24%), whereas the Ag-nitrate TFC (20%) and Ag-acetate TFC (11%) membranes experienced significantly smaller declines. The flux recovery ratios were 69%, 77%, and 89% for the pristine TFC, Ag-nitrate TFC, and Ag-acetate TFC membranes, respectively, indicating that both Ag-MAFs-functionalized membranes had superior resistance to BSA fouling compared to the pristine TFC membrane. BSA molecules tend to adhere to the membrane surface via hydrophobic interactions.<sup>87</sup> As indicated by contact angle measurements, the Ag-MAFs-functionalized membranes displayed higher hydrophilicity. The presence of Ag-MAFs nanoparticles on the membrane surface enhanced hydrophilicity, thereby reducing the adsorption of BSA molecules. This improved hydrophilicity contributed to the superior antiprotein fouling performance of the Ag-MAFs-functionalized membranes.

Figure 8c shows the biofouling results for pristine TFC and Ag-MAFs functionalized TFC membranes. Compared to BSA fouling, all membranes experienced a more significant flux decline. This greater flux decline during the biofouling experiment is attributed to the nutrient-rich environment created by LB broth (500 ppm) and PBS solution (100 mM) in the feedwater. These conditions promote aggressive biofilm formation, involving both bacteria and extracellular polymeric substances (EPS), leading to more severe membrane fouling than observed with the lower concentration of BSA (100 ppm). However, the Ag-MAFs functionalized membrane exhibited a smaller flux decline than the pristine TFC membrane, indicating reduced biofilm formation. Additionally, the functionalized membranes showed higher flux recovery ratios compared to the pristine TFC membrane, with recovery rates of 62.3%, 69.5%, and 71.6% for the pristine TFC, Ag-nitrate TFC, and Ag-acetate TFC membranes, respectively. This improvement is attributed to the strong antibacterial activity of Ag-MAFs nanoparticles, which inhibit biofilm formation and growth. The fouling rate and flux recovery ratio fall in the order of Ag-acetate TFC > Ag-nitrate TFC > pristine TFC. The Ag-MAFs membranes

**Table 3. Different Ag-Based Antibacterial Agents and Approaches Applied for the Fabrication of Anti-Biofouling Polyamide TFC RO Membranes; a Comparison of Surface Properties, Antibacterial Activity, Antibacterial Mechanisms, and Operational Performance<sup>a</sup>**

support	antibacterial agent	modification approach	AFM	hydrophilicity	zeta	antibacterial assessment method	biofoulant/antibacterial activity	operational performance	refs
MPD/TMC	tannic acid and Ag NPs	surface grafting and impregnation	11% increase	12% decline	-16.9	cfu, fluorescence microscopy	E. coli of 100%, S. aureus	ROS generation and damage to the structure of bacterial cells	90
MPD/TMC	Ag NPs/PDA biomimetic nanoparticles (BNPs)	in-situ surface deposition	23% increase	64% increase	-27	cfu, inhibition zone	E. coli and S. aureus of ~100%	enhanced water permeability (>2 times) and salt rejection (by 2% of 98%) improved FRR of 98% for SA and 96% for BSA	91
commercial TFC-PA	Ag NPs	in-situ surface decoration	NA	21% increase	NA	cfu	E. coli	the release of Ag <sup>+</sup> ions. Improved water flux (24%) with high rejection (>99%) lower flux decline (30% decrease) during fouling test	89
FilmTec SW30XLE	Ag NPs/CNCs	in-situ decoration of Ag NPs on CNCs deposited PDA incorporation	28% increase	8% increase	NA	cfu, CLSM	E. coli of 90%	physical stress under direct contact of CNCs with bacteria. Release of Ag <sup>+</sup> ions. Improved water permeability (15.6%) with significant loss of salt rejection	14
MPD/TMC	silver sulfide (Ag <sub>2</sub> S)	in-situ deposition	42% increase	38% increase	NA	cfu	E. coli of 49%	release of Ag <sup>+</sup> ions. Binding of Ag <sup>+</sup> ions with thiol functional groups of proteins. Increased water flux (2.5%) with high salt rejection (>98%)	92
MPD/TMC	Ag NPs@SiO <sub>2</sub>	in-situ deposition	NA	20% increase	NA	cfu, fluorescence microscopy	E. coli of 92.7%, P. aeruginosa of 99.5%, S. aureus of 73.3%	release of Ag <sup>+</sup> ions and DNA replication disruption. ROS generation and ATP production disruption. Slight water flux decline (by 3%) with 98.8% salt rejection after immobilization	93
Commercial polyamide SWC4+	Ag NPs	direct incorporation by arc plasma	NA	60% increase	NA	cfu, CLSM	E. coli of 95%, P. aeruginosa of 80%, S. aureus of 85%	contact killing and penetration into the cell. ROS generation and DNA damage structure. Release of Ag <sup>+</sup> ions. 40% initial increased flux while maintaining salt rejection, 9.5% decreased water flux with almost unchanged salt rejection for 10 days after Ag NPs incorporation	94
FilmTec SW30XLE	Ag NPs	in-situ formation	7% increase	17% decrease	No change	cfu, CLSM	E. coli of 78%, P. aeruginosa of 91%, S. aureus of 96%	release of Ag <sup>+</sup> ions. Slight reduction of water permeability (up to 17%) with no obvious effect on salt rejection after Ag NPs deposition	34
FilmTec commercial RO	Ag NPs coated PDA	in-situ reduction	NA	45% increase	no change	cfu	E. coli of 42.4%, B. subtilis of 62.7%	release of Ag <sup>+</sup> ion. Reduced water flux (nearly 20%) and enhanced salt rejection after modification	13
MPD/TMC	tannic acid/Ag NPs complex	grafting	32% decline	60% increase	NA	inhibition zone	E. coli & S. aureus	the presence of numerous phenolic hydroxyl groups. Enhanced water flux of 20.57 LMH (60%) and 97.8% salt rejection (~3%)	10
MPD/TMC	Ag-MAFs	in-situ formation	almost similar	32% decline	increased positively	SEM, CLSM	E. coli of 99%	release of Ag <sup>+</sup> ions and amino-benzimidazole linker. Contact killing and binding of Ag <sup>+</sup> ions with thiol functional groups of proteins. Enhanced water flux (45%) and no significant salt reduction (97.6%)	this study

<sup>a</sup>Colony forming unit (cfu), confocal laser scanning microscopy (CLSM), cellulose nanocrystals (CNCs), adenosine triphosphate (ATP), bovine serum albumin (BSA), flux recovery ratio (FRR).

effectively prevent biofilm formation by combining the sustained release of Ag<sup>+</sup> ions and amino-benzimidazole linkers, which disrupt bacterial membranes, cellular functions, and adhesion.

For polyamide TFC membranes, surface hydrophilicity and chemical properties play a crucial role in determining their fouling behavior. A more hydrophilic surface effectively reduces organic fouling by promoting the formation of a hydration layer, which decreases the deposition of hydrophobic foulants.<sup>60</sup> When the hydrolyzed acyl chloride groups of the TFC layer react with Ag ions, the resulting Ag-MAFs cover the carboxylic groups, reducing the number of active carboxyl groups on the membrane surface and consequently minimizing foulant deposition and accumulation.<sup>88</sup> Furthermore, the hydrophilic amine groups, such as amino-benzimidazole, within Ag-MAF nanostructures attract water molecules through hydrogen bonding, creating a hydration layer that prevents BSA adsorption and accumulation.<sup>60,88</sup>

**4.8. Performance Benchmarking.** Table 3 presents a comparative overview of various techniques for surface modification of reverse osmosis TFC membranes using Ag-based materials. Table 3 lists the antibacterial agents, surface treatment methods, key physicochemical parameters, the type of biofoulant, and an evaluation of operational performance and antibacterial mechanisms. Most research studies aim to enhance antibacterial properties and biofouling resistance while maintaining separation performance. Ngo et al.<sup>89</sup> decorated Ag nanoparticles in-situ, achieving a 21% increase in hydrophilicity and, consequently, a 24% improvement in water flux. Focusing on biofouling resistance, Jackson et al. functionalized commercial reverse osmosis membranes with cellulose nanocrystals (CNCs) and Ag nanoparticles, resulting in an 8% increase in hydrophilicity and a 15.6% increase in water permeability with a trade-off of significant salt rejection loss.<sup>14</sup> Ben-Sasson et al.<sup>34</sup> formed Ag NPs in-situ on commercial RO membrane surfaces, leading to a reduced permeability of up to 17%. While these studies highlight significant advancements, there remains room for further optimization, particularly in enhancing water flux through careful adjustment of Ag-based agent impregnation. The surface functionalization of Ag-MAFs membranes developed in this study achieved superior water flux increases without compromising salt rejection, while also significantly enhancing antibacterial activity and improving antibiofouling performance compared to the pristine TFC membrane. The promising outcomes of this study underscore the potential of Ag-MAFs functionalization for tailored surface modifications, offering platforms with enhanced antibiofouling and antibacterial properties, accompanied by excellent salt rejection and water permeability. The in-situ complexation of Ag NPs with tannic acid (TA) improved membrane performance in terms of antibacterial, antifouling, and antibiofouling tendency, with reduced biofilm formation.<sup>90</sup>

## 5. CONCLUSION

The in-situ surface functionalization successfully achieved a uniform distribution of novel Ag-MAFs on the active sites of the TFC membrane surface, resulting in excellent antibacterial and antibiofouling properties. Techniques such as FTIR, XPS, and EDX confirmed the successful formation and growth of Ag-MAFs on the polyamide surface. The Ag-MAFs demonstrated strong stability and attachment, as validated by leaching tests. The novel Ag-MAFs nanoparticles, containing amine functional groups, significantly improved surface hydrophilicity, water flux, and antibacterial activity with minimal impact on salt rejection.

Both Ag-MAFs-modified membranes maintained stable permeate flux over an 8 h filtration period, indicating the integrity and stability of the selective layer. The robust crystal structure of Ag-MAFs minimized the leakage of Ag ions, enhancing both stability and antibacterial properties without compromising permeability or separation efficiency. Confocal imaging revealed approximately 99% antibacterial activity, significantly reducing live bacterial cells and enhancing biofouling resistance. In summary, the modified membranes offer a promising solution for long-term antibacterial performance and resistance to bio/organic fouling in filtration systems.

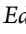
## ■ ASSOCIATED CONTENT


### Data Availability Statement


The data underlying this study are publicly available at the time of publication.

## ■ AUTHOR INFORMATION

### Corresponding Authors

**Pooria Karami** – Department of Mechanical Engineering, 10-241 Donadeo Innovation Center for Engineering, Advanced Water Research Lab (AWRL), University of Alberta, Edmonton, Alberta T6G 1H9, Canada;  [orcid.org/0000-0001-5532-6882](https://orcid.org/0000-0001-5532-6882); Email: [pkarami@ualberta.ca](mailto:pkarami@ualberta.ca)


**David Wishart** – Department of Biological Sciences, University of Alberta, Edmonton, Alberta T6G 2E9, Canada; Department of Computing Science, University of Alberta, Edmonton, Alberta T6G 2E8, Canada;  [orcid.org/0000-0002-3207-2434](https://orcid.org/0000-0002-3207-2434); Email: [dwishart@ualberta.ca](mailto:dwishart@ualberta.ca)

**Mohtada Sadrzadeh** – Department of Mechanical Engineering, 10-241 Donadeo Innovation Center for Engineering, Advanced Water Research Lab (AWRL), University of Alberta, Edmonton, Alberta T6G 1H9, Canada;  [orcid.org/0000-0002-0403-8351](https://orcid.org/0000-0002-0403-8351); Email: [sadrzade@ualberta.ca](mailto:sadrzade@ualberta.ca)

### Authors

**Seyedeh Fatemeh Seyedpour** – Department of Mechanical Engineering, 10-241 Donadeo Innovation Center for Engineering, Advanced Water Research Lab (AWRL), University of Alberta, Edmonton, Alberta T6G 1H9, Canada; Department of Biological Sciences, University of Alberta, Edmonton, Alberta T6G 2E9, Canada

**Saeed Khoshhal Salestan** – Department of Mechanical Engineering, 10-241 Donadeo Innovation Center for Engineering, Advanced Water Research Lab (AWRL), University of Alberta, Edmonton, Alberta T6G 1H9, Canada; Department of Chemistry and Chemical Engineering, Chalmers University of Technology, Gothenburg 412 96, Sweden

**Sadegh Aghapour Aktij** – Department of Chemical & Materials Engineering, Donadeo Innovation Centre for Engineering, University of Alberta, Edmonton, Alberta T6G 1H9, Canada; Department of Mechanical Engineering, 10-241 Donadeo Innovation Center for Engineering, Advanced Water Research Lab (AWRL), University of Alberta, Edmonton, Alberta T6G 1H9, Canada;  [orcid.org/0000-0002-7802-2686](https://orcid.org/0000-0002-7802-2686)

**Upasana Singh** – Department of Biological Sciences, University of Alberta, Edmonton, Alberta T6G 2E9, Canada

**Suyenna Huang** – Department of Biological Sciences, University of Alberta, Edmonton, Alberta T6G 2E9, Canada

Jia Wei Chew – Department of Chemistry and Chemical Engineering, Chalmers University of Technology, Gothenburg 412 96, Sweden; [orcid.org/0000-0002-6603-1649](https://orcid.org/0000-0002-6603-1649)

Ahmad Rahimpour – Department of Chemical & Materials Engineering, Donadeo Innovation Centre for Engineering, University of Alberta, Edmonton, Alberta T6G 1H9, Canada; [orcid.org/0009-0006-6658-9809](https://orcid.org/0009-0006-6658-9809)

Complete contact information is available at:  
<https://pubs.acs.org/10.1021/acsomega.5c02816>

## Notes

The authors declare no competing financial interest.

## ACKNOWLEDGMENTS

The financial support for this work by the Natural Science and Engineering Research Council of Canada (NSERC), Canada's Oil Sands Innovation Alliance (COSIA), and Alberta Innovates is gratefully acknowledged.

## REFERENCES

- (1) Khorshidi, B.; Shabani, S.; Sadzadeh, M. Prospects of nanocomposite membranes for water treatment by osmotic-driven membrane processes. In *Nanocomposite Membranes for Water and Gas Separation*; Elsevier, 2020; pp 257–297.
- (2) Cadotte, J.; King, R.; Majerle, R.; Petersen, R. Interfacial synthesis in the preparation of reverse osmosis membranes. *J. Macromol. Sci.-Chem.* **1981**, *15* (5), 727–755.
- (3) Gu, J.-E.; Jun, B.-M.; Kwon, Y.-N. Effect of chlorination condition and permeability of chlorine species on the chlorination of a polyamide membrane. *Water Res.* **2012**, *46* (16), 5389–5400.
- (4) Hibbs, M. R.; McGrath, L. K.; Kang, S.; Adout, A.; Altman, S. J.; Elimelech, M.; Cornelius, C. J. Designing a biocidal reverse osmosis membrane coating: Synthesis and biofouling properties. *Desalination* **2016**, *380*, 52–59.
- (5) Jiang, S.; Li, Y.; Ladewig, B. P. A review of reverse osmosis membrane fouling and control strategies. *Sci. Total Environ.* **2017**, *595*, 567–583.
- (6) Kochkodan, V.; Hilal, N. A comprehensive review on surface modified polymer membranes for biofouling mitigation. *Desalination* **2015**, *356*, 187–207.
- (7) Mauter, M. S.; Wang, Y.; Okemgbo, K. C.; Osuji, C. O.; Giannelis, E. P.; Elimelech, M. Antifouling ultrafiltration membranes via post-fabrication grafting of biocidal nanomaterials. *ACS Appl. Mater. Interfaces* **2011**, *3* (8), 2861–2868.
- (8) Ray, J. R.; Tadepalli, S.; Nergiz, S. Z.; Liu, K.-K.; You, L.; Tang, Y.; Singamaneni, S.; Jun, Y.-S. Hydrophilic, bactericidal nanohetero-enabled reverse osmosis membranes to improve fouling resistance. *ACS Appl. Mater. Interfaces* **2015**, *7* (21), 11117–11126.
- (9) Hegab, H. M.; ElMekawy, A.; Barclay, T. G.; Michelmore, A.; Zou, L.; Saint, C. P.; Ginic-Markovic, M. Fine-tuning the surface of forward osmosis membranes via grafting graphene oxide: performance patterns and biofouling propensity. *ACS Appl. Mater. Interfaces* **2015**, *7* (32), 18004–18016.
- (10) Suresh, D.; Goh, P. S.; Ismail, A. F.; Mansur, S. B.; Wong, K. C.; Asraf, M. H.; Malek, N. A. N. N.; Wong, T. W. Complexation of tannic acid/silver nanoparticles on polyamide thin film composite reverse osmosis membrane for enhanced chlorine resistance and anti-biofouling properties. *Desalination* **2022**, *543*, 116107.
- (11) (a) Karami, P.; Khorshidi, B.; Shamaei, L.; Beaulieu, E.; Soares, J. O. B.; Sadzadeh, M. Nanodiamond-enabled thin-film nanocomposite polyamide membranes for high-temperature water treatment. *ACS Appl. Mater. Interfaces* **2020**, *12* (47), 53274–53285. (b) Karami, P.; Khorshidi, B.; Soares, J. B.; Sadzadeh, M. Fabrication of highly permeable and thermally stable reverse osmosis thin film composite polyamide membranes. *ACS Appl. Mater. Interfaces* **2020**, *12* (2), 2916–2925.
- (12) Yun, J.; Lee, D. G. Silver nanoparticles: a novel antimicrobial agent. In *Antimicrobial Nanoarchitectonics*; Elsevier, 2017; pp 139–166.
- (13) Yang, Z.; Wu, Y.; Wang, J.; Cao, B.; Tang, C. Y. In situ reduction of silver by polydopamine: A novel antimicrobial modification of a thin-film composite polyamide membrane. *Environ. Sci. Technol.* **2016**, *50* (17), 9543–9550.
- (14) Jackson, J. C.; Camargos, C. H.; Liu, C.; Martinez, D. S.; Paula, A. J.; Rezende, C. A.; Faria, A. F. Antimicrobial activity of thin-film composite membranes functionalized with cellulose nanocrystals and silver nanoparticles via one-pot deposition and layer-by-layer assembly. *Environ. Sci.:Water Res. Technol.* **2024**, *10*, 639–651.
- (15) Yin, J.; Yang, Y.; Hu, Z.; Deng, B. Attachment of silver nanoparticles (AgNPs) onto thin-film composite (TFC) membranes through covalent bonding to reduce membrane biofouling. *J. Membr. Sci.* **2013**, *441*, 73–82.
- (16) Mafuné, F.; Kohno, J.-y.; Takeda, Y.; Kondow, T.; Sawabe, H. Structure and stability of silver nanoparticles in aqueous solution produced by laser ablation. *J. Phys. Chem. B* **2000**, *104* (35), 8333–8337.
- (17) Marambio-Jones, C.; Hoek, E. M. A review of the antibacterial effects of silver nanomaterials and potential implications for human health and the environment. *J. Nanopart. Res.* **2010**, *12*, 1531–1551.
- (18) (a) Rahaman, M. S.; Thérien-Aubin, H.; Ben-Sasson, M.; Ober, C. K.; Nielsen, M.; Elimelech, M. Control of biofouling on reverse osmosis polyamide membranes modified with biocidal nanoparticles and antifouling polymer brushes. *J. Mater. Chem. B* **2014**, *2* (12), 1724–1732. (b) Wu, J.; Yu, C.; Li, Q. Regenerable antimicrobial activity in polyamide thin film nanocomposite membranes. *J. Membr. Sci.* **2015**, *476*, 119–127.
- (19) Mozafari, M.; Seyedpour, S. F.; Salestan, S. K.; Rahimpour, A.; Shamsabadi, A. A.; Firouzjaei, M. D.; Esfahani, M. R.; Tiraferri, A.; Mohsenian, H.; Sangermano, M.; et al. Facile Cu-BTC surface modification of thin chitosan film coated polyethersulfone membranes with improved antifouling properties for sustainable removal of manganese. *J. Membr. Sci.* **2019**, *588*, 117200.
- (20) Seyedpour, S. F.; Arabi Shamsabadi, A.; Khoshhal Salestan, S.; Dadashi Firouzjaei, M.; Sharifian Gh, M.; Rahimpour, A.; Akbari Afkhami, F.; Shirzad Kebria, M. R.; Elliott, M. A.; Tiraferri, A.; et al. Tailoring the biocidal activity of novel silver-based metal azolate frameworks. *ACS Sustain. Chem. Eng.* **2020**, *8* (20), 7588–7599.
- (21) Niehues, M.; Erker, G.; Kehr, G.; Schwab, P. F.; Fröhlich, R.; Blacque, O.; Berke, H. Synthesis and Structural Features of Arduengo Carbene Complexes of Group 4 Metallocene Cations. *Organometallics* **2002**, *21*, 2905–2911.
- (22) Díez-González, S.; Nolan, S. P. Stereoelectronic parameters associated with N-heterocyclic carbene (NHC) ligands: a quest for understanding. *Coord. Chem. Rev.* **2007**, *251* (5–6), 874–883.
- (23) Cavallo, L.; Correa, A.; Costabile, C.; Jacobsen, H. Steric and electronic effects in the bonding of N-heterocyclic ligands to transition metals. *J. Organomet. Chem.* **2005**, *690* (24–25), 5407–5413.
- (24) Samantaray, M. K.; Pang, K.; Shaikh, M. M.; Ghosh, P. From large 12-membered macrometallacycles to ionic (NHC) 2M+ Cl– type complexes of gold and silver by modulation of the N-substituent of amido-functionalized N-heterocyclic carbene (NHC) ligands. *Inorg. Chem.* **2008**, *47* (10), 4153–4165.
- (25) (a) Chernousova, S.; Epple, M. Silver as antibacterial agent: ion, nanoparticle, and metal. *Angew. Chem., Int. Ed.* **2013**, *52* (6), 1636–1653. (b) Yu, L.; Zhang, Y.; Zhang, B.; Liu, J. Enhanced antibacterial activity of silver nanoparticles/halloysite nanotubes/graphene nanocomposites with sandwich-like structure. *Sci. Rep.* **2014**, *4*, 4551.
- (26) Tonelli, M.; Simone, M.; Tasso, B.; Novelli, F.; Boido, V.; Sparatore, F.; Paglietti, G.; Pricl, S.; Giliberti, G.; Blois, S.; et al. Antiviral activity of benzimidazole derivatives. II. Antiviral activity of 2-phenylbenzimidazole derivatives. *Bioorg. Med. Chem.* **2010**, *18* (8), 2937–2953.
- (27) Kumar, U.; Narang, R.; Nayak, S. K.; Singh, S. K.; Gupta, V. Benzimidazole: structure activity relationship and mechanism of action as antimicrobial agent. *Res. J. Pharm. Technol.* **2017**, *10* (7), 2400–2414.

- (28) (a) Barcin, T.; Yucel, M. A.; Ersan, R. H.; Alagoz, M. A.; Dogen, A.; Burmaoglu, S.; Algul, O. Deep learning approach to the discovery of novel bisbenzazole derivatives for antimicrobial effect. *J. Mol. Struct.* **2024**, *1295*, 136668. (b) Abdel-Wahab, B. F.; Abdel-Latif, E.; Mohamed, H. A.; Awad, G. E. Design and synthesis of new 4-pyrazolin-3-yl-1, 2, 3-triazoles and 1, 2, 3-triazol-4-yl-pyrazolin-1-ylthiazoles as potential antimicrobial agents. *Eur. J. Med. Chem.* **2012**, *52*, 263–268.
- (29) Kondo, S.; Miura, T. Reaction-diffusion model as a framework for understanding biological pattern formation. *science* **2010**, *329* (5999), 1616–1620.
- (30) Tiraferri, A.; Elimelech, M. Direct quantification of negatively charged functional groups on membrane surfaces. *J. Membr. Sci.* **2012**, *389*, 499–508.
- (31) Tiraferri, A.; Kang, Y.; Giannelis, E. P.; Elimelech, M. Highly hydrophilic thin-film composite forward osmosis membranes functionalized with surface-tailored nanoparticles. *ACS Appl. Mater. Interfaces* **2012**, *4* (9), S044–S053.
- (32) Pejman, M.; Dadashi Firouzjaei, M.; Aghapour Aktij, S.; Das, P.; Zolghadr, E.; Jafarian, H.; Arabi Shamsabadi, A.; Elliott, M.; Sadrzadeh, M.; Sangermano, M.; et al. In situ Ag-MOF growth on pre-grafted zwitterions imparts outstanding antifouling properties to forward osmosis membranes. *ACS Appl. Mater. Interfaces* **2020**, *12* (32), 36287–36300.
- (33) Werner, P.-E.; Eriksson, L.; Westdahl, M. TREOR, a semi-exhaustive trial-and-error powder indexing program for all symmetries. *J. Appl. Crystallogr.* **1985**, *18* (5), 367–370.
- (34) Ben-Sasson, M.; Lu, X.; Bar-Zeev, E.; Zodrow, K. R.; Nejati, S.; Qi, G.; Giannelis, E. P.; Elimelech, M. In situ formation of silver nanoparticles on thin-film composite reverse osmosis membranes for biofouling mitigation. *Water Res.* **2014**, *62*, 260–270.
- (35) Seyedpour, S. F.; Dadashi Firouzjaei, M.; Rahimpour, A.; Zolghadr, E.; Arabi Shamsabadi, A.; Das, P.; Akbari Afkhami, F.; Sadrzadeh, M.; Tiraferri, A.; Elliott, M. Toward sustainable tackling of biofouling implications and improved performance of TFC FO membranes modified by Ag-MOF nanorods. *ACS Appl. Mater. Interfaces* **2020**, *12* (34), 38285–38298.
- (36) Porcelli, N.; Judd, S. Chemical cleaning of potable water membranes: A review. *Sep. Purif. Technol.* **2010**, *71* (2), 137–143.
- (37) Peng, Y.; Yang, J.; Qi, H.; Li, H.; Li, S.; Su, B.; Han, L. 2D COFs interlayer manipulated interfacial polymerization for fabricating high performance reverse osmosis membrane. *Sep. Purif. Technol.* **2022**, *303*, 122198.
- (38) Jung, C. H.; Lee, M.-S.; Kim, D. Y.; Shin, M. G.; An, S.; Kang, D.-K.; Kim, J. F.; Nam, S.-E.; Park, S.-J.; Lee, J.-H. Biopolymer-supported thin-film composite membranes for reverse osmosis. *Chem. Eng. J.* **2025**, *S05*, 159264.
- (39) Ben-Sasson, M.; Zodrow, K. R.; Gengeng, Q.; Kang, Y.; Giannelis, E. P.; Elimelech, M. Surface functionalization of thin-film composite membranes with copper nanoparticles for antimicrobial surface properties. *Environ. Sci. Technol.* **2014**, *48* (1), 384–393.
- (40) Naghshbandi, Z.; Gholinejad, M.; Sansano, J. M.; Eskandari, M. Graphene quantum dots incorporated ZIF-67 for stabilization of Au nanoparticles: Efficient catalyst for A3-coupling and nitroarenes reduction reactions. *Appl. Organomet. Chem.* **2024**, *38* (4), No. e7400.
- (41) Sundaraganesan, N.; Ilakiamani, S.; Subramani, P.; Joshua, B. D. Comparison of experimental and ab initio HF and DFT vibrational spectra of benzimidazole. *Spectrochim. Acta, Part A* **2007**, *67* (3–4), 628–635.
- (42) Bellamy, L. *The Infrared Spectra of Complex Molecules*; Springer Science & Business Media, 2013.
- (43) Liu, D.; Jiang, F.; Zhang, T.; Yu, C.; Hu, Z.; Zhang, L.; Shi, S. A DOPO-based reactive flame retardant containing benzimidazole groups: Synthesis and its flame-retardation on epoxy resin. *J. Appl. Polym. Sci.* **2024**, *141* (5), No. e54890.
- (44) Naghshbandi, Z.; Gholinejad, M.; Sansano, J. M. Novel magnetic zeolitic imidazolate framework for room temperature enhanced catalysis. *Inorg. Chem. Commun.* **2023**, *150*, 110463.
- (45) (a) Nespolo, M.; Aroyo, M. I. *International Tables for Crystallography, Vol. A, Space-group symmetry*. Wiley, 2016. Pp. xxi + 873. Price GBP 295.00, EUR 354.00 (hardcover). ISBN 978-0-470-97423-0. *Acta Crystallogr., Sect. A: Found. Adv.* **2017**, *73* (3), 274–276. (b) Kittel, C. *Introduction to Solid State Physics*, 8th ed.; John Wiley & Sons, 2021.
- (46) Gupta, A. K.; Salazar, D. M.; Orthaber, A. Solvent and Counter-Ion Induced Coordination Environment Changes Towards AgI Coordination Polymers. *Eur. J. Inorg. Chem.* **2019**, *2019* (33), 3740–3744.
- (47) Liu, H.-Y.; Wu, H.; Yang, J.; Liu, Y.-Y.; Liu, B.; Liu, Y.-Y.; Ma, J.-F. pH-Dependent assembly of 1D to 3D octamolybdate hybrid materials based on a new flexible bis-[(pyridyl)-benzimidazole] ligand. *Cryst. Growth Des.* **2011**, *11* (7), 2920–2927.
- (48) Li, X.-P.; Zhang, J.-Y.; Pan, M.; Zheng, S.-R.; Liu, Y.; Su, C.-Y. Zero to three dimensional increase of silver (I) coordination assemblies controlled by deprotonation of 1, 3, 5-tri (2-benzimidazolyl) benzene and aggregation of multinuclear building units. *Inorg. Chem.* **2007**, *46* (11), 4617–4625.
- (49) Melaiye, A.; Sun, Z.; Hindi, K.; Milsted, A.; Ely, D.; Reneker, D. H.; Tessier, C. A.; Youngs, W. J. Silver (I)–imidazole cyclophane gem-diol complexes encapsulated by electrospun tephophilic nanofibers: Formation of nanosilver particles and antimicrobial activity. *J. Am. Chem. Soc.* **2005**, *127* (7), 2285–2291.
- (50) Baig, M. I.; Ingole, P. G.; Choi, W. K.; Jeon, J.-d.; Jang, B.; Moon, J. H.; Lee, H. K. Synthesis and characterization of thin film nanocomposite membranes incorporated with surface functionalized Silicon nanoparticles for improved water vapor permeation performance. *Chem. Eng. J.* **2017**, *308*, 27–39.
- (51) Silverstein, R. M.; Webster, F. X.; Kiemle, D. J.; Bryce, D. L. *Spectrometric Identification of Organic Compounds*; John Wiley & Sons, 2014.
- (52) Khorshidi, B.; Thundat, T.; Fleck, B.; Sadrzadeh, M. Thin film composite polyamide membranes: parametric study on the influence of synthesis conditions. *RSC Adv.* **2015**, *5* (68), 54985–54997.
- (53) (a) Benavente, J.; Vázquez, M. Effect of age and chemical treatments on characteristic parameters for active and porous sublayers of polymeric composite membranes. *J. Colloid Interface Sci.* **2004**, *273* (2), 547–555. (b) Boussu, K.; De Baerdemaeker, J.; Dauwe, C.; Weber, M.; Lynn, K. G.; Depla, D.; Aldea, S.; Vankelecom, I. F.; Vandecasteele, C.; Van der Bruggen, B. Physico-chemical characterization of nanofiltration membranes. *ChemPhysChem* **2007**, *8* (3), 370–379. (c) Tang, C. Y.; Kwon, Y.-N.; Leckie, J. O. Probing the nano- and micro-scales of reverse osmosis membranes—a comprehensive characterization of physicochemical properties of uncoated and coated membranes by XPS, TEM, ATR-FTIR, and streaming potential measurements. *J. Membr. Sci.* **2007**, *287* (1), 146–156.
- (54) Tang, C. Y.; Kwon, Y.-N.; Leckie, J. O. Effect of membrane chemistry and coating layer on physicochemical properties of thin film composite polyamide RO and NF membranes: II. Membrane physicochemical properties and their dependence on polyamide and coating layers. *Desalination* **2009**, *242* (1), 168–182.
- (55) Ederer, J.; Janoš, P.; Ecorchard, P.; Tolasz, J.; Štengl, V.; Beneš, H.; Perchacz, M.; Pop-Georgievski, O. Determination of amino groups on functionalized graphene oxide for polyurethane nanomaterials: XPS quantitation vs. functional speciation. *RSC Adv.* **2017**, *7* (21), 12464–12473.
- (56) (a) Park, S.-H.; Kim, S. H.; Park, S.-J.; Ryoo, S.; Woo, K.; Lee, J. S.; Kim, T.-S.; Park, H.-D.; Park, H.; Park, Y.-I.; et al. Direct incorporation of silver nanoparticles onto thin-film composite membranes via arc plasma deposition for enhanced antibacterial and permeation performance. *J. Membr. Sci.* **2016**, *513*, 226–235. (b) Omi, F. R.; Rastgar, M.; Mohseni, M.; Singh, U.; Dilokekunakul, W.; Keller, R.; Wishart, D.; Wessling, M.; Davis Vecitis, C.; Sadrzadeh, M. Removal of emerging contaminants from water using novel electroconductive membranes in a hybrid membrane distillation and electro-Fenton process. *Sep. Purif. Technol.* **2025**, *357*, 130083.

- (57) Elimelech, M.; Phillip, W. A. The future of seawater desalination: energy, technology, and the environment. *science* **2011**, *333* (6043), 712–717.
- (58) Zhou, Z.; Mukherjee, S.; Warnan, J.; Li, W.; Wannapaiboon, S.; Hou, S.; Rodewald, K.; Rieger, B.; Weidler, P. G.; Wöll, C.; et al. Porphyrin based metal–organic framework films: nucleation and growth. *J. Mater. Chem. A* **2020**, *8* (48), 25941–25950.
- (59) Rana, D.; Matsuura, T. Surface modifications for antifouling membranes. *Chem. Rev.* **2010**, *110* (4), 2448–2471.
- (60) Tiraferri, A.; Kang, Y.; Giannelis, E. P.; Elimelech, M. Superhydrophilic thin-film composite forward osmosis membranes for organic fouling control: fouling behavior and antifouling mechanisms. *Environ. Sci. Technol.* **2012**, *46* (20), 11135–11144.
- (61) Vrijenhoek, E. M.; Hong, S.; Elimelech, M. Influence of membrane surface properties on initial rate of colloidal fouling of reverse osmosis and nanofiltration membranes. *J. Membr. Sci.* **2001**, *188* (1), 115–128.
- (62) (a) Werber, J. R.; Osuji, C. O.; Elimelech, M. Materials for next-generation desalination and water purification membranes. *Nat. Rev. Mater.* **2016**, *1*, 16018. (b) Zhu, J.; Qin, L.; Uliana, A.; Hou, J.; Wang, J.; Zhang, Y.; Li, X.; Yuan, S.; Li, J.; Tian, M.; et al. Elevated Performance of Thin Film Nanocomposite Membranes Enabled by Modified Hydrophilic MOFs for Nanofiltration. *ACS Appl. Mater. Interfaces* **2017**, *9* (2), 1975–1986.
- (63) (a) Firouzjaei, M. D.; Shamsabadi, A. A.; Aktij, S. A.; Seyedpour, S. F.; Sharifian Gh, M.; Rahimpour, A.; Esfahani, M. R.; Ulbricht, M.; Soroush, M. Exploiting synergetic effects of graphene oxide and a silver-based metal–organic framework to enhance antifouling and anti-biofouling properties of thin-film nanocomposite membranes. *ACS Appl. Mater. Interfaces* **2018**, *10* (49), 42967–42978. (b) Rahimpour, A.; Seyedpour, S. F.; Aghapour Aktij, S.; Dadashi Firouzjaei, M.; Zirehpour, A.; Arabi Shamsabadi, A.; Khoshhal Salestan, S.; Jabbari, M.; Soroush, M. Simultaneous Improvement of Antimicrobial, Antifouling, and Transport Properties of Forward Osmosis Membranes with Immobilized Highly-Compatible Polyrhodanine Nanoparticles. *Environ. Sci. Technol.* **2018**, *52*, 5246–5258.
- (64) (a) Ben-Sasson, M.; Lu, X.; Bar-Zeev, E.; Zodrow, K. R.; Nejati, S.; Qi, G.; Giannelis, E. P.; Elimelech, M. In situ formation of silver nanoparticles on thin-film composite reverse osmosis membranes for biofouling mitigation. *Water Res.* **2014**, *62*, 260–270. (b) Ben-Sasson, M.; Zodrow, K. R.; Gengeng, Q.; Kang, Y.; Giannelis, E. P.; Elimelech, M. Surface functionalization of thin-film composite membranes with copper nanoparticles for antimicrobial surface properties. *Environ. Sci. Technol.* **2014**, *48* (1), 384–393.
- (65) Soroush, A.; Ma, W.; Cyr, M.; Rahaman, M. S.; Asadishad, B.; Tufenkji, N. In situ silver decoration on graphene oxide-treated thin film composite forward osmosis membranes: biocidal properties and regeneration potential. *Environ. Sci. Technol. Lett.* **2016**, *3* (1), 13–18.
- (66) (a) Hindi, K. M.; Siciliano, T. J.; Durmus, S.; Panzner, M. J.; Medvetz, D. A.; Reddy, D. V.; Hogue, L. A.; Hovis, C. E.; Hilliard, J. K.; Mallet, R. J.; et al. Synthesis, stability, and antimicrobial studies of electronically tuned silver acetate N-heterocyclic carbenes. *J. Med. Chem.* **2008**, *51* (6), 1577–1583. (b) Gordon, O.; Vig Slenters, T. n.; Brunetto, P. S.; Villaruz, A. E.; Sturdevant, D. E.; Otto, M.; Landmann, R.; Fromm, K. M. Silver coordination polymers for prevention of implant infection: thiol interaction, impact on respiratory chain enzymes, and hydroxyl radical induction. *Antimicrob. Agents Chemother.* **2010**, *54* (10), 4208–4218.
- (67) (a) Taheri, M.; Ashok, D.; Sen, T.; Enge, T. G.; Verma, N. K.; Tricoli, A.; Lowe, A.; R Nisbet, D.; Tsuzuki, T. Stability of ZIF-8 nanopowders in bacterial culture media and its implication for antibacterial properties. *Chem. Eng. J.* **2021**, *413*, 127511. (b) Li, M.; Zhu, L.; Lin, D. Toxicity of ZnO nanoparticles to *Escherichia coli*: mechanism and the influence of medium components. *Environ. Sci. Technol.* **2011**, *45* (5), 1977–1983.
- (68) Qin, Z.; Zheng, Y.; Wang, Y.; Du, T.; Li, C.; Wang, X.; Jiang, H. Versatile roles of silver in Ag-based nanoalloys for antibacterial applications. *Coord. Chem. Rev.* **2021**, *449*, 214218.
- (69) Wyszogrodzka, G.; Marszalek, B.; Gil, B.; Dorozynski, P. Metal-organic frameworks: mechanisms of antibacterial action and potential applications. *Drug Discovery Today* **2016**, *21* (6), 1009–1018.
- (70) (a) Berchel, M.; Gall, T. L.; Denis, C.; Hir, S. L.; Quentel, F.; Elléouet, C.; Montier, T.; Rueff, J.-M.; Salaün, J. Y.; Haelters, J.-P.; et al. A silver-based metal–organic framework material as a reservoir of bactericidal metal ions. *New J. Chem.* **2011**, *35* (5), 1000–1003. (b) Lu, X.; Ye, J.; Zhang, D.; Xie, R.; Bogale, R. F.; Sun, Y.; Zhao, L.; Zhao, Q.; Ning, G. Silver carboxylate metal–organic frameworks with highly antibacterial activity and biocompatibility. *J. Inorg. Biochem.* **2014**, *138*, 114–121.
- (71) (a) Eckhardt, S.; Brunetto, P. S.; Gagnon, J.; Priebe, M.; Giese, B.; Fromm, K. M. Nanobio silver: its interactions with peptides and bacteria, and its uses in medicine. *Chem. Rev.* **2013**, *113* (7), 4708–4754. (b) Zhang, W.; Ye, G.; Liao, D.; Chen, X.; Lu, C.; Nezamzadeh-Ejhi, A.; Khan, M. S.; Liu, J.; Pan, Y.; Dai, Z. Recent advances of silver-based coordination polymers on antibacterial applications. *Molecules* **2022**, *27* (21), 7166.
- (72) Seyedpour, S. F.; Arabi Shamsabadi, A.; Khoshhal Salestan, S.; Dadashi Firouzjaei, M.; Sharifian Gh, M.; Rahimpour, A.; Akbari Afkhami, F.; Shirzad Kebria, M. r.; Elliott, M. A.; Tiraferri, A.; et al. Tailoring the Biocidal Activity of Novel Silver-Based Metal Azolate Frameworks. *ACS Sustain. Chem. Eng.* **2020**, *8*, 7588–7599.
- (73) (a) Dale, A. G.; Porcu, A.; Mann, J.; Neidle, S. The mechanism of resistance in *Escherichia coli* to ridimilazole and other antibacterial head-to-head bis-benzimidazole compounds. *Med. Chem. Res.* **2022**, *31* (7), 1176–1191. (b) Keri, R. S.; Hiremathad, A.; Budagumpi, S.; Nagaraja, B. M. Comprehensive review in current developments of benzimidazole-based medicinal chemistry. *Chem. Biol. Drug Des.* **2015**, *86* (1), 19–65.
- (74) Sridevi, C.; Kannan, M. M.; Abhinayani, G.; Sravya, N. Designing and Biological Evaluation of new benzimidazole compounds. *Chem. Sci. Trans.* **2013**, *2* (922), 926.
- (75) Song, D.; Ma, S. Recent development of benzimidazole-containing antibacterial agents. *ChemMedChem* **2016**, *11* (7), 646–659.
- (76) Zhang, L.; Addla, D.; Ponmani, J.; Wang, A.; Xie, D.; Wang, Y.-N.; Zhang, S.-L.; Geng, R.-X.; Cai, G.-X.; Li, S.; et al. Discovery of membrane active benzimidazole quinolones-based topoisomerase inhibitors as potential DNA-binding antimicrobial agents. *Eur. J. Med. Chem.* **2016**, *111*, 160–182.
- (77) Liao, Z.-Q.; Dong, C.; Carlson, K. E.; Srinivasan, S.; Nwachukwu, J. C.; Chesnut, R. W.; Sharma, A.; Nettles, K. W.; Katzenellenbogen, J. A.; Zhou, H.-B. Triaryl-substituted Schiff bases are high-affinity subtype-selective ligands for the estrogen receptor. *J. Med. Chem.* **2014**, *57* (8), 3532–3545.
- (78) Ivask, A.; ElBadawy, A.; Kaweeteerawat, C.; Boren, D.; Fischer, H.; Ji, Z.; Chang, C. H.; Liu, R.; Tolaymat, T.; Telesca, D.; et al. Toxicity mechanisms in *Escherichia coli* vary for silver nanoparticles and differ from ionic silver. *ACS Nano* **2014**, *8* (1), 374–386.
- (79) Ivask, A.; Suarez, E.; Patel, T.; Boren, D.; Ji, Z.; Holden, P.; Telesca, D.; Damoiseaux, R.; Bradley, K. A.; Godwin, H. Genome-wide bacterial toxicity screening uncovers the mechanisms of toxicity of a cationic polystyrene nanomaterial. *Environ. Sci. Technol.* **2012**, *46* (4), 2398–2405.
- (80) (a) Cui, L.; Chen, P.; Chen, S.; Yuan, Z.; Yu, C.; Ren, B.; Zhang, K. In situ study of the antibacterial activity and mechanism of action of silver nanoparticles by surface-enhanced Raman spectroscopy. *Anal. Chem.* **2013**, *85* (11), 5436–5443. (b) Stoimenov, P. K.; Klinger, R. L.; Marchin, G. L.; Klabunde, K. J. Metal oxide nanoparticles as bactericidal agents. *Langmuir* **2002**, *18* (17), 6679–6686.
- (81) Izakmehri, Z.; Ardjmand, M.; Ganji, M. D.; Babanezhad, E.; Heydarinasab, A. Removal of dioxane pollutants from water by using Al-doped single walled carbon nanotubes. *RSC Adv.* **2015**, *5* (59), 48124–48132.
- (82) Miao, W.; Wang, J.; Liu, J.; Zhang, Y. Self-cleaning and antibacterial zeolitic imidazolate framework coatings. *Adv. Mater. Interfaces* **2018**, *5* (14), 1800167.

(83) (a) Banerjee, I.; Pangule, R. C.; Kane, R. S. Antifouling coatings: recent developments in the design of surfaces that prevent fouling by proteins, bacteria, and marine organisms. *Adv. Mater.* **2011**, *23* (6), 690–718. (b) Liu, C.; Lee, J.; Ma, J.; Elimelech, M. Antifouling thin-film composite membranes by controlled architecture of zwitterionic polymer brush layer. *Environ. Sci. Technol.* **2017**, *51* (4), 2161–2169.

(84) Idarraga-Mora, J. A.; Lemelin, M. A.; Weinman, S. T.; Husson, S. M. Effect of short-term contact with C1–C4 monohydric alcohols on the water permeance of MPD-TMC thin-film composite reverse osmosis membranes. *Membranes* **2019**, *9* (8), 92.

(85) (a) Ludwig, H. *Reverse Osmosis Seawater Desalination Vol. 2: Planning, Process Design and Engineering—A Manual for Study and Practice*; Springer Nature, 2022. (b) Wang, X.-N.; Liu, Y.; Pan, X.-H.; Han, J.-X.; Hao, J. Parameters for seawater reverse osmosis product water: a review. *Expo. Health* **2017**, *9*, 157–168.

(86) (a) Lau, W. J.; Gray, S.; Matsuura, T.; Emadzadeh, D.; Paul Chen, J.; Ismail, A. F. A review on polyamide thin film nanocomposite (TFN) membranes: History, applications, challenges and approaches. *Water Res.* **2015**, *80*, 306–324. (b) Wen, Y.; Yuan, J.; Ma, X.; Wang, S.; Liu, Y. Polymeric nanocomposite membranes for water treatment: a review. *Environ. Chem. Lett.* **2019**, *17* (4), 1539–1551.

(87) Ye, G.; Lee, J.; Perreault, F.; Elimelech, M. Controlled architecture of dual-functional block copolymer brushes on thin-film composite membranes for integrated “defending” and “attacking” strategies against biofouling. *ACS Appl. Mater. Interfaces* **2015**, *7* (41), 23069–23079.

(88) Shen, L.; Zhang, X.; Zuo, J.; Wang, Y. Performance enhancement of TFC FO membranes with polyethyleneimine modification and post-treatment. *J. Membr. Sci.* **2017**, *534*, 46–58.

(89) Ngo, T. H. A.; Huy Do, H.; Thanh Pham, H.; Dinh Do, K.; Dao, D. S.; Nghia Pham, N. Antibacterial and Antifouling Properties of Ag- and Cu-Decorated Thin Film Composite Polyamide Reverse Osmosis Membranes. *ChemNanoMat* **2023**, *9* (6), No. e202300004.

(90) Suresh, D.; Goh, P. S.; Wong, T. W.; Zhang, L.; Ismail, A. F. In-situ complexation of silver nanoparticle on thin film composite reverse osmosis membrane for improving desalination and anti-biofouling performance. *Desalination* **2024**, *569*, 117040.

(91) Huo, H.-Q.; Mi, Y.-F.; Yang, X.; Lu, H.-H.; Ji, Y.-L.; Zhou, Y.; Gao, C.-J. Polyamide thin film nanocomposite membranes with in-situ integration of multiple functional nanoparticles for high performance reverse osmosis. *J. Membr. Sci.* **2023**, *669*, 121311.

(92) Nchoe, O. B.; Matshetshe, K.; As’ Ballim, M.; Tetyana, P.; Sikhwivhilu, K.; Moloto, N. Fabrication of  $f_2$ -incorporated polyamide thin film nanocomposite reverse osmosis membranes with antifouling properties. *J. Appl. Polym. Sci.* **2023**, *140* (41), No. e54524.

(93) Park, S.-H.; Ko, Y.-S.; Park, S.-J.; Lee, J. S.; Cho, J.; Baek, K.-Y.; Kim, I. T.; Woo, K.; Lee, J.-H. Immobilization of silver nanoparticle-decorated silica particles on polyamide thin film composite membranes for antibacterial properties. *J. Membr. Sci.* **2016**, *499*, 80–91.

(94) Park, S.-H.; Kim, S. H.; Park, S.-J.; Ryoo, S.; Woo, K.; Lee, J. S.; Kim, T.-S.; Park, H.-D.; Park, H.; Park, Y.-I.; et al. Direct incorporation of silver nanoparticles onto thin-film composite membranes via arc plasma deposition for enhanced antibacterial and permeation performance. *J. Membr. Sci.* **2016**, *513*, 226–235.